

Received: 15 February 2021

Revised: 7 October 2021

Accepted: 19 October 2021

Addressing planar solid oxide cell degradation mechanisms: A critical review of selected components

Stephen J. McPhail¹  | Stefano Frangini¹ | Jérôme Laurencin² | Elisa Effori² | Amira Abaza² | Aiswarya Krishnakumar Padinjarethil³ | Anke Hagen³ | Aline Léon⁴ | Annabelle Brisse⁴ | Daria Vladikova⁵ | Blagoy Burdin⁵ | Fiammetta Rita Bianchi⁶ | Barbara Bosio⁶ | Paolo Piccardo⁷ | Roberto Spotorno⁷ | Hiroyuki Uchida⁸  | Pierpaolo Polverino⁹ | Ennio Andrea Adinolfi⁹ | Fabio Postiglione¹⁰ | Jong-Ho Lee¹¹ | Hamza Moussaoui¹² | Jan Van herle¹²

¹ ENEA, Agenzia Nazionale per le Nuove Tecnologie, L'Energia e lo Sviluppo Economico Sostenibile, Rome, Italy

² Univ. Grenoble Alpes – CEA/LITEN, Grenoble, France

³ DTU Energy, Technical University of Denmark, Kgs. Lyngby, Denmark

⁴ EIFER, European Institute for Energy Research, Karlsruhe, Germany

⁵ IEES, Institute of Electrochemistry and Energy Systems, Bulgarian Academy of Science, Sofia, Bulgaria

⁶ Department of Civil, Chemical and Environmental Engineering, University of Genoa, Genova, Italy

⁷ Department of Chemistry and Industrial Chemistry, University of Genoa, Genova, Italy

⁸ Clean Energy Research Center, University of Yamanashi, Kofu, Japan

⁹ Department of Industrial Engineering, University of Salerno, Fisciano, Italy

¹⁰ Department of Information and Electrical Engineering and Applied Mathematics (DEIM), University of Salerno, Fisciano, Italy

¹¹ Korea Institute of Science and Technology (KIST) and University of Science and Technology (UST), Seoul, Korea

¹² Ecole Polytechnique Fédérale de Lausanne (EPFL), Faculty of Engineering (STI), Inst. Mech. Eng (IGM), Group of Energy Materials (GEM), Sion, Switzerland

Correspondence

Stephen J McPhail, Via Anguillarese 301,
00123 Rome, Italy.

Email: stephen.mcphail@enea.it

Abstract

In this review paper, a critical assessment of the main degradation processes in three key components of solid oxide fuel cells and electrolyzers (negative and positive electrodes and the interconnect) is undertaken, attempting prioritization of respective degradation effects and recommendation of the best approaches in their experimental ascertainment and numerical modeling. Besides different approaches to quantifying the degradation rate of an operating solid oxide cell (SOC), the latest advancements in microstructural representation (3D imaging and reconstruction) of SOC electrodes are reviewed, applied to the quantification of triple-phase boundary (TPB) lengths and morphology evolution over time. The intrinsic degradation processes in the negative (fuel)

This is an open access article under the terms of the [Creative Commons Attribution-NonCommercial](https://creativecommons.org/licenses/by-nc/4.0/) License, which permits use, distribution and reproduction in any medium, provided the original work is properly cited and is not used for commercial purposes.

© 2021 The Authors. *Electrochemical Science Advances* published by Wiley-VCH GmbH.

electrode and the positive (oxygen) electrode are discussed, covering first the composition and governing mechanisms of the respective electrodes, followed by a comprehensive evaluation of the most important factors of degradation during operation. By this systematic identification of dominant degradation processes, measurement techniques, and modeling approaches, the foundations are laid for the definition of meaningful accelerated stress testing of SOC cells and stacks, which will help the technology achieve the constantly more demanding durability targets in market applications.

KEYWORDS

degradation, electrode processes, interconnect degradation, lumped modelling, multi-scale modelling, review, solid oxide electrolysis, solid oxide fuel cells

1 | INTRODUCTION

The history of solid oxide cells (SOC) starts with the discovery of the relatively high ionic conductivity of the so-called Nernst mass – yttria-doped zirconia – at elevated temperatures (600–1000°C).¹ The first application of this property is in the generation of electric power from gaseous fuel (solid oxide fuel cell, SOFC), starting in the 1930s with the work of Swiss scientists Baur and Preis,² thereafter gaining momentum in the 1970s. The first concept of solid oxide electrolysis cell (SOEC, the reverse operation of SOFC) was reported in the late 1960s.³ SOEC stacks were developed within the HOT Elly project, sponsored by the German Federal Ministry of Research and Technology (BMFT).⁴ The option to operate the same device alternately for electricity production and electrolysis is a characteristic, unique feature of high-temperature fuel cells and is currently most mature in SOC systems.

SOCs hold great potential and may have an important role in the energy transition to fossil-free energy systems thanks to this dual nature, providing the opportunity for massive integration of renewable (both electric and biogenic) energy sources into the overall energy system, in the pursuit of a low-carbon, energy-efficient economy.^{5,6} However, before their deployment across the spectrum of potential applications is made possible by large-scale manufacturing, certain technical challenges such as durability (i.e., maintenance-free achievement of application-specific lifetimes) and component cost reduction have to be overcome.

Considering an expected useful commercial lifetime of 80,000–90,000 hours for stationary applications,^{7,8} the objective is to maintain the initial performance for as long as possible and to minimize progressive degradation of all system components.

SOC stack degradation is influenced by multiple factors within the window of operating conditions. The initial performance decreases over SOC lifetime due to the effect of use (electrochemical ageing), of time (calendar aging), of different permanent, and/or accidental stress conditions (thermal cycling, current load, mechanical wearing, imperfect conditioning, poisoning, etc.). Degradation also affects the constituent components differently and at different time-scales. Therefore, prioritization of effects is needed based on a failure mode analysis to be able to address the key mechanisms toward ever more robust and durable SOC systems.

1.1 | Origin and objectives of this review

The authors of this review are collaborating within the framework of a dedicated project on accelerated stress test (AST) protocols for SOC stacks, funded by the European Fuel Cells and Hydrogen Joint Undertaking (FCH JU). The project, AD ASTRA (HArnessing Degradation mechanisms to prescribe Accelerated Stress Tests for the Realization of SOC lifetime prediction Algorithms), brings together key European research organizations and industries, with input from project leaders on similar topics in the United States, Japan, and South Korea, to address this most challenging of objectives. Both fuel cell (combined heat and power) and electrolysis (power-to-X) operation are considered. More information on the project approach and emerging results can be found at www.ad-astra.eu.

This review aims at presenting the current state-of-knowledge concerning SOC degradation phenomena, mechanisms, and modeling approaches, addressing both SOFC and SOEC operation modes. It is set up to be a critical assessment of the main findings in the literature. Building up from reviews that already list the vast compendium

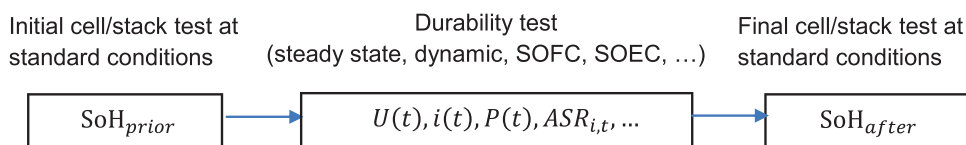


FIGURE 1 Illustration of durability testing and data extraction

of degradation mechanisms, usually specifically for SOFCs (e.g., refs. 9–11), it attempts prioritization of the degradation effects identified and recommendation of the best approaches in the experimental and numerical harnessing of the associated mechanisms at the microscale and stack level. It acts as a foundation on which to build test procedures that accelerate incumbent degradation in a scientifically meaningful, or at least technologically acceptable, way. By systematically addressing the findings from previous studies on degradation processes – experimental and numerical – and combining these with in-depth study of stacks operated in the field, it is aimed to prioritize those components and those mechanisms that govern the long-term performance of SOC stacks, and design test procedures that isolate these lifetime-inhibiting states, streamlining characterization and facilitating in-operando lifetime prediction, while recognizing differences between stacks and single (or button) cells, as marked in ref. 7.

Thus, after exploring in depth the possible definitions of the degradation rate and ambiguities in its quantification, in theory and in experimental practice, a review will be presented of the main degradation processes in three key components of the SOC: the negative and positive electrodes and the interconnect. The effects of microscale degradation processes are reviewed for their compound influence at stack level, considering their representation through both multi-scale modeling and simplified, lumped models.

1.2 | Definitions of degradation

Degradation is the decrease of the performance of the SOC over time: specifically, and simplistically, power output for given fuel input in SOFC operation, and fuel output for given power input in SOEC operation. There are several options to quantify this parameter using either explicit or implicit parameters. Typical degradation tests are carried out by starting with an initial characterization of the cell/stack performance, or state-of-health (SoH), followed by the durability test at constant or dynamic conditions, and finishing by a final performance characterization of SoH (see Figure 1). The test data recorded during these test sequences are used for quantifying degradation.

Voltage (U), current density (i), area specific resistance (ASR), or power output (P) measured during cell/stack

operation have been commonly used as degradation parameters.

The degradation rate (DR) is then defined as the rate at which a cell's performance deteriorates over time according to a specific performance indicator. It is commonly expressed in the following units: mV/kh, mV%/kh, mΩ cm²/kh, or mΩ cm²%/kh. Most often, long-term durability tests are performed at constant current and the change in the corresponding voltage (normalized to 1000 operation hours, in %) is used for the definition of the DR, see equation (1):

$$DR = \left| \frac{U(i, t) - U(i, t = 0)}{U(i, t = 0)} \right| \times \frac{1000}{t} \times 100\% \quad (1)$$

where $U(i, t = 0)$ is the initial cell voltage at current density i and $U(i, t)$ is the cell voltage at current density i after the operating time t (in hours).

As a consequence of degradation, the cell voltage $U(i, t)$ decreases in SOFC mode and increases in SOEC mode during the operating period t . The processes leading to this change can have different origins, which are summarized in the following terms of the instantaneous cell voltage $U(i, t)$, equation (2).¹²

$$U(i, t) = U_{rev} - iR_i + (\eta_{Act}^{pos} - \eta_{Act}^{neg}) + (\eta_{Conc}^{pos} - \eta_{Conc}^{neg}) \quad (2)$$

In this equation, the average current density i is considered negative by convention in electrolysis mode ($i < 0$) and positive in fuel cell mode ($i > 0$). The term U_{rev} refers to the “thermodynamic” or “reversible” voltage given by the Nernst equation¹. It corresponds to the open circuit voltage (OCV) at standard concentrations and a second contribution due to the reversible losses (depending only on the operating conditions defined by the temperature, the current density and the gas feeding conditions, including gas leaks).

The other terms are related to the irreversible phenomena arising upon operation. They include the ohmic losses for which R_i denotes the ohmic resistances for each cell

¹ $E = E^0 - \frac{RT}{zF} \ln Q$ where E is the reversible (Nernst) voltage (U_{rev} in Equation 2), E^0 the electrochemical potential difference of the electrons in the two electrodes, and the last term defines the effects of concentration differences, with Q being the reaction quotient of products and reactants.

component and the contact resistance between the interfaces (such as between electrodes and interconnects). The terms η_{Act} and η_{Conc} are the activation and concentration overpotentials at the positive and negative electrodes, which combine all the processes occurring in the active layers, including the reactions of charge transfer. Concentration overpotentials are attributed to the mass transfer limitation across the porous electrodes (i.e., diffusion of the gas species to the reaction sites).

In calculating the DR, instead of using the voltage change (Equation 1), the change of the corresponding area specific resistance (ASR, Equation 3) may be used. The selection of ASR as the characteristic parameter for the DR is to be preferred, as it allows for comparison of tests carried out under different conditions such as at galvanostatic (constant current density) and potentiostatic (constant voltage) conditions.^{13–16} The ASR is defined as:

$$ASR(i, t) = \left| \frac{U(i + \delta i, t) - U(i, t)}{\delta i} \right| \quad (3)$$

where δi is a differential change in the current density around the reference current. The absolute value is chosen so that the physical meaning of the term is preserved in both electrolysis and fuel cell mode. For the calculation of the ASR, instead of δi , often the (constant) operating current density i is used and instead of $U(i + \delta i, t)$, the U at OCV, because they are easier to obtain. The DR is then calculated as:

$$DR = \frac{(ASR_{(i,t)} - ASR_{(i,t=0)})}{ASR_{(i,t=0)}} \times \frac{1000}{t} \times 100\% \quad (4)$$

The linearized approach described above presents some challenges. First of all, the value of the DR depends on the selected parameter: a DR based on a differential current change in Equation (3) is typically smaller than a DR based on the voltage loss compared to OCV in Equation (3) at typical current densities and in typical degradation ranges. Furthermore, a DR could be calculated based on the absolute change in cell or stack voltage (U instead of ASR) in Equation (4), leading to still different values. Therefore, the adopted calculation route for given DR values needs to be specified.

A linearized average DR over the selected testing period(s) does not always represent the real voltage degradation trend. It omits the deviations that may occur due to different kinetics of degradation processes during the operating period(s). The effects due to changes in current density, reactant/product composition, temperature, and pressure are not expressed explicitly, making it difficult to compare tests where these operating conditions have undergone variations. The timescales over which the DR is calcu-

lated are not standardized and can range from a few hundred hours to several years, which makes fair comparisons between different test series or studies difficult.^{16–22}

In reality, the change of power output, ASR or voltage over time is often parabolic, with a faster DR in the initial phase and a slower DR over the long term.^{22,23} This trend, which is well-known in the field of reliability engineering, is a result of different degradation mechanisms with different reaction rates at the interfaces of the electrodes. A solution is to execute the tests for sufficiently long times to compensate for the fast initial degradation or to “condition” the cells and stack before the durability test to exclude the fast initial DR from the actual durability test.²⁴

The absolute degradation rate yields the DR at a specific time and is calculated as shown in Equation (5), where i_s is the steady state current value at which the cell is operated during the time interval ($t-t_0$). Within this time interval, the DR can also be defined as an average degradation rate or, for an infinitesimal time change, as an instantaneous value of DR depending on the focus of the study.^{13,15,16}

$$DR(t) [\%/h] = 100 \times \left(\frac{dASR(i_s, t) \times i_s / dt}{U(i_s, t_0)} \right) \quad (5)$$

This approach relies on the steady state of the current i_s and identifies the degradation in *performance* of the cell.

Another approach is to consider a “cell-specific property,” determined at identical “reference” conditions, that is, a certain temperature and gas composition, in particular at OCV. Thus, a comparison can be made between the “state” of the degraded cell or stack after finishing the durability test (SoH_{after}) and the “initial state,” before the test (SoH_{prior}), characterized under the same “standard” conditions (see Figure 1 for illustration). This approach avoids the uncertainties arising from the nonlinear behavior of the degradation. Furthermore, it enables the direct comparison of resultant DRs of tests under greatly varying conditions, such as SOFC or SOEC mode, galvanostatic (at constant current density), potentiostatic (at constant voltage), dynamic, or reversible conditions, different operating temperatures, fuels, and so on. At OCV the state of the cell is governed primarily by temperature and gas composition. An ASR at $i = 0$, calculated according to Equation (3), is however very much biased toward the gas conversion impedance, less sensible in terms of gas diffusion impedance, and therefore not reliable nor relevant for the cell performance under current. In ref. 14, a different approach is therefore proposed, defining a reference state of the cell based on a different interpretation of the ASR (named ASR_{OCV}), which here will be called SoH (state of health) to avoid confusion with the ASR as the slope of the iV -curve at the operating point. The definition of this state of the cell SoH also allows comparing performances of dif-

ferent cells directly and can include detailed deconvolution of the contributions from electrodes, electrolyte, and so on. The cell-specific property SoH is defined in ref. 24 as:

$$\text{SoH} = \frac{U_{\text{OCV}} - U(i)}{i} \quad (6)$$

where $U(i)$ is the voltage at a certain current density i from the iV curve. The DR (normalized to 1000 h operating time in %) is then calculated according to Equation (7), where SoH is measured at OCV at “reference” conditions.

$$\text{DR} = \frac{(\text{SoH}_{\text{after}} - \text{SoH}_{\text{prior}})}{\text{SoH}_{\text{prior}}} \times \frac{1000}{t} \times 100\% \quad (7)$$

$\text{SoH}_{\text{prior}}$ is determined before starting the durability test and $\text{SoH}_{\text{after}}$ after finishing the durability period, both at the same set of conditions, from iV curves (or electrochemical impedance spectroscopy, EIS). Hence, an intrinsic value of the degradation is obtained without directly taking into account the change of cell/stack output parameters over time, linear or non-linear trends, or other deviations that are likely to occur within a real long-term test.

Lowest DRs currently reported for SOFCs at cell and stack level are below 1% kh^{-1} based on cell or stack voltage.²² For SOECs, the DR value is typically around 2% kh^{-1} or smaller.^{18,25,26}

The current target for SOFC operation in stationary applications is about 0.1% based on stack voltage.^{18,20,27–29} These degradation rates mean that the voltage change is in the range of about 0.8 mV/1000 h at constant current and an assumed cell voltage of around 0.8 V. Such small changes are difficult to measure with sufficient accuracy unless tests are carried out for sufficiently long times, exceeding several thousand hours. Efforts have been devoted to detect small changes of the cell/stack parameters in shorter test times by the application of more precise analytical techniques. One such approach was developed and verified in the project ENDURANCE, increasing sensitivity in the evaluation of the degradation rate.^{30–31} It is based on shape analysis of the current-voltage (iV) curves, which are sensitive to operating conditions and degradation. Differential resistance analysis (DRA) is based on the calculated derivative $R_{d,k} = dU_k/di_k$ for every point of the iV curve. It constitutes a new functional dependence, $R_{d,k} = f(i_k)$, using the minimum of the differential resistance $R_{d,\min}$ as a performance indicator, which is determined by the intrinsic state of the system, that is, its state of health (not necessarily as defined in Equation 6), and not by the external conditions as current or potential. The operation with derivatives increases the sensitivity of the analysis since changes in $R_{d,\min}$ caused by the state of the system will become observable much earlier than those of

other parameters selected for monitoring and evaluation of degradation. The iV characteristics and the calculation of $R_{d,\min}$ should be performed periodically, that is, in 100, 500, or 1000 hours, or at the beginning and at the end of the test, independently of operating conditions between two measurements. Then, the degradation rate DR can be expressed as:

$$\text{DR} = \left(\frac{R_{d,\min}(t) - R_{d,\min}(t=0)}{R_{d,\min}(t=0)} \right) \times \frac{1000}{t} \times 100\% \quad (8)$$

1.3 | Complexity of degradation and durability evaluation

There are several long-term tests reported, also exceeding 75,000 hours for SOFC,²⁷ but most of these are performed in the laboratory environment. There is a big difference when testing is performed for fundamental studies, usually on small or button cells, or for precommercial evaluation.³² Besides, performance behavior depends not only on mere scaling but also on the selected cell/stack architecture (including fabrication processes), the test fixture, precision of the measurement instrumentation, geometrical factors, pre-conditioning, operating conditions, and dynamics, stress factors. A step forward is the development of procedures and harmonized protocols, which should ensure as much as possible replicable and comparable results. Differences cannot be avoided, but equivalent experimental approaches will help to apply results obtained in different laboratories. In the frame of the European Fuel Cells and Hydrogen Joint Undertaking (FCH JU), dedicated projects were funded to converge towards validated and harmonized testing and characterization procedures: both the ENDURANCE database²⁹ and the SOCTESQA test procedures²⁸ are freely available for use, and were instrumental in the development of IEC standards on SOC testing.^{33,34}

For the improvement of SOC long-term performance and optimization of SOC architectures, it is important to identify and quantify the degradation sources before the development of successful mitigation strategies. However, as already pointed out, the assessment of SOC lifetime is time consuming and thus expensive. Several years of extensive laboratory testing combined with field experiments under actual application conditions are needed. Another challenge is the analysis of tested cells concerning the physical failure mechanisms, as it is difficult to identify the dominant degradation process.

The general approach is to combine long-term testing, which evaluates the total degradation coming from all the components (electrodes, electrolyte, interfaces, barrier

layers, etc.), with additional periodic electrochemical testing: current-voltage (i - V) characteristics, which give the integral picture of the system's capability to produce electrical energy, combined with EIS in selected working points, which can evaluate components in the overall degradation. A specialized approach is the use of segmented single repeating unit (SRU) testing including local EIS (on each electrode segment), which allows to pinpoint the local character of degradation phenomena and to couple this with targeted post-test analysis.^{35,36} The final stage of such a complex study is post-mortem analysis, which visualizes some of the morphological and compositional changes due to degradation effects.^{17,37}

Repetitive and systematic long-term operation of various SOFC stacks (5000 to 30,000 h) in the Japanese NEDO project, combined with detailed post-test analyses on microscopic changes, have resulted in significant improvement of SOFC durability.^{7,10,11} In the frame of that project, shorter tests have also been performed for detection of small changes by application of more precise analytical techniques.³⁸ Similar approaches for decrease of the testing time are set out in refs. 30 and 31. Another approach is the performance of dedicated studies of components degradation *ex situ* (anode, cathode, interconnect, etc.). However, their behavior in the cell/stack assembly may strongly differ due to the specific operational environment, where the influence of other (adjacent) components will be significant, but the scope is to isolate a dominating degradation source and assess its response to different operating conditions.

For instance, in ref. 22, a long-term study on cell level combining electrochemical testing with post-test analysis is performed for extracting information about the behavior of the two electrodes at different temperatures and current densities. The integrated result gives a lower degradation rate at higher temperatures, even at high current density. Analysis shows the domination of the positive electrode (lanthanum strontium manganite/yttria-stabilized zirconia LSM/YSZ) degradation at a higher current density and lower temperature and of the negative electrode (Ni-YSZ) at a higher temperature. This observation brings to the conclusion that the negative electrode degradation is less detrimental to the cell performance than that of the positive electrode for fuel cell operating conditions of this generation of cells. In ref. 24, ASR contributions from the different cell components (electrodes and electrolyte) in pristine and degraded cells were evaluated as a function of the operating conditions (temperature, current density, steam in the fuel, fuel utilization). The dominating increase of the ASR in cells with LSCF (lanthanum strontium cobalt ferrite)/GDC (gadolinia-doped ceria) positive electrodes was found to come from the Ni-YSZ negative electrode, which is strongly influenced by the overall steam content.

The role of operating conditions on the occurrence and influence of degradation sources is clearly important and has been assessed using electrochemical models as well.³⁹ In refs. 40 and 41, an electrochemical model was put forward valid over a wide range of operating conditions and supporting the implementation of degradation phenomena. It used a two-dimensional model of the cell and interconnection system, a distinction between the two common oxygen electrode materials LSM and LSCF, and estimated model parameters calibrated through experimental data obtained in segmented setups. Included phenomena were (i) interconnect corrosion, (ii) loss of YSZ ionic conductivity, (iii) nickel particle growth in the Ni-YSZ negative electrode, (iv) chromium contamination, and (v) insulating phase formation. The positive electrode largely contributed to the degradation of the chosen set of materials and conditions. Local overpotential governed chromium contamination, which in turn could promote the formation of insulating phases, as operation proceeds. Qualitative agreement with experimental data was achieved without dedicated adjustments of the parameters, allowing also lifetime prediction.

To quantify degradation of a given cell to predict total lifetime in a justified manner, extensive testing and characterization should be performed at different operation conditions and transformed into a model. Experimental data are also necessary for model validation and should be obtained at cell/stack level recording the influence of operating parameters. EIS is a powerful tool for this separation.

The development of sophisticated algorithms and tools for multi-scale assessment of performance from cell to system level – as in ref. 42 – cannot avoid long-term tests (several years) to mimic real operation. The results of the NEDO project described above^{11–38} arise from evaluation under conditions in which heat or flow distribution is well controlled, in optimized stack design and under rated operation conditions. However, these large-scale campaigns are less appropriate for iterative optimization of new materials, architecture or operating modes, nor convenient for day-to-day implementation in a SOC development company. Furthermore, “academic” assessments have limitations since the degradation rate in laboratory-tested cells is usually larger than in industrially delivered stacks.

To obviate the problem of long-term experimental tests simulating real operation, accelerated stress tests (AST) need to be introduced. This method is still under active development and the experimental conditions should activate the same degradation mechanisms as in non-accelerated testing. This should not lead to irreversible collateral changes, which may lead to false results when extrapolated to regular operation, especially considering the lower degradation in the system environment. Sophisticated performance models incorporating degradation

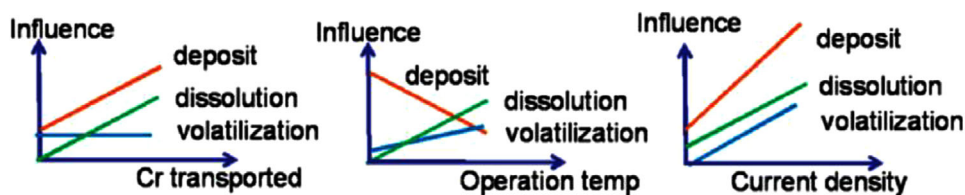


FIGURE 2 Influence of operating conditions on processes dominating Cr-poisoning of SOFC oxygen electrodes⁴³

functions need to validate the achieved “state of degradation” and quantify the accelerating impact of the test. To avoid non-representative exacerbation of other phenomena, the selection of the aggravating conditions is critical.

The degradation mechanisms operating in a complex electrochemical system are highly convoluted and quasi-chaotic – or at least stochastic – in nature. For example, extensive studies on the effects on SOC positive electrodes of chromium evaporation from hot steel components have shown that aggravating different test input parameters leads to diverging responses of the governing mechanisms (dissolution of Cr species in the perovskite phase, deposition, and electrochemical volatilization of Cr species on active sites), see Figure 2.⁴³ From the trends depicted in Figure 2, only varying current density could generate a coherent variation of the mechanisms (though the slight divergence of influences would need to be taken into account).

Furthermore, the close-knit processes in a working SOC often lead to domino-effects, whereby acute degradation occurring in one component or area can trigger or accelerate degradation elsewhere in the stack. In ref. 40, a deconvolution approach (based on EIS) is applied for separation of the negative electrode, positive electrode, and electrolyte degradation as a function of the temperature, which, however, produces different side effects: the introduction of other accelerated degradation processes as poisoning, carbon deposition, and so on, or enhanced temporal performance by improved contacts. Nakajo et al.^{39,44} clearly demonstrated how SOFC degradation depends on stack and system design and operation. A stack model investigating the impact of the operating conditions on SOFC lifetime predicted the acceleration of degradation due to the sequential activation of multiple processes. Requirements for the highest system efficiency at start and at long-term differ. Operation at a lower specific power and higher stack temperature extended the lifetime by a factor up to 10, because a beneficial decrease in cathodic overpotential in SOFC prevailed over other degradation processes.

Thus, it is crucial to identify the critical locations and dominant mechanisms that curtail SOC lifetime (see Section 2). The major factors that influence the degradation of SOCs are temperature, current density, thermal cycling,

redox, load cycling, and poisoning from reactant contaminants, and their effects are under intensive study.

Operation protocols for ASTs should be carefully designed, especially for operation at high temperatures. The AST in ref. 45 revealed that at high temperatures the chemical and structural deterioration accelerated by increasing temperature is compensated by the facilitated reaction and transport kinetics. The experiments in refs. 46 and 47 aim at selecting the optimal operation profiles for accelerated stress tests. Ploner et al.¹⁴ evaluated 180 durability tests at different operating conditions (temperature, current density, steam in the fuel, fuel utilization) to select the accelerating conditions for negative electrode aging.

In ASTs, the lifetime data obtained from the aggravated test conditions are extrapolated to normal operating conditions employing a model, which fits the data to an appropriate lifetime distribution function to project remaining useful life at normal operating conditions. Since one of the critical factors in ASTs is that the studied degradation mechanism should not change on aggravation of the test parameters, it is important to understand it at different operating conditions to predict such mechanism in proper models. Validated with experimental data, these models act as useful tools for knowing and addressing the degradation of SOCs. In turn, this understanding and prioritization of, and capability to harness degradation mechanisms to accelerate them in a controlled manner, will benefit SOC component manufacturers and industry by significantly reducing acceptance test times, thereby accelerating quality improvement and increasing competitiveness of their products. However, at the moment the AST approach is in an early stage of development with a distinct lack of publications.

2 | COMPONENT-LEVEL DEGRADATION

The combined and convoluted effects of degradation must be approached systematically to identify and work on the mechanisms that are critical. A first deconvolution of the problem follows the different components of the SOC single repeating unit: negative and positive electrodes, electrolyte, interconnect, and sealing (Figure 3). Failure in one

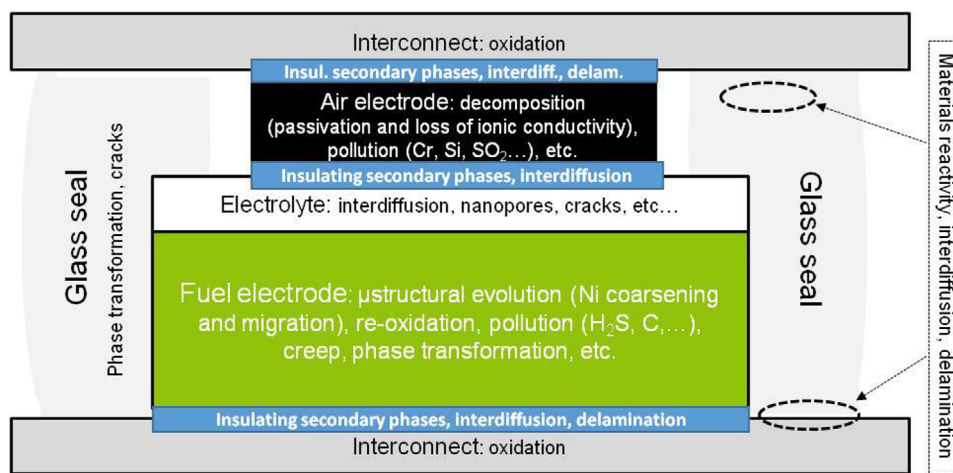


FIGURE 3 Main degradation phenomena arising in the different components of the SOC single repeating unit

of these components may correlate with failure in the others (e.g., seal tightness and reoxidation of Ni in the negative electrode are interlinked and it is difficult to determine the initial degradation source). Approaching a compound failure mechanism may be easier by addressing one component rather than another (for reasons of cost, complexity, accessibility, or others), which creates a set of trade-offs in prioritizing the component to focus development on. The authors, based on the joint discussion in the project AD ASTRA of relevant scientific knowledge and field operation experience, have established three components to be critical in overall SOC degradation, with the following effects (see also Figure 3):

- **Negative (fuel) electrode:** Microstructural evolution such as nickel agglomeration (densification), nickel depletion (volatilization) in both modes, and reoxidation in SOFC mode
- **Positive (oxygen) electrode:** Material decomposition and reactivity with the electrolyte (e.g., formation of isolating phases), delamination (in both modes), electrode microcracking due to composition changes in SOEC mode, and chromium poisoning in SOFC mode
- **Interconnect:** Contact loss, especially at the oxygen electrode side due to long-term thermal oxidation (corrosion) and degradation of protective coating layer properties (occurring in both electrolysis and fuel cell modes), solid-state diffusion in the contacting layers including the sealing.

The selection above does not imply that degradation does not occur in the electrolyte or other functional layers or the seals, nor that failure in these latter components does not cause rapid performance deterioration. Indeed, the degradation of the conductivity of YSZ electrolyte due to the tetragonal transformation has been identified by the

diffusion of yttrium and the internal reduction of NiO, the actual kinetics of which strongly depended on the fabrication procedures of cell/stacks.^{10,11} Furthermore, the interfaces between components are often the main areas where instabilities initiate and propagate (see Figure 3 and, e.g., ref. 48). However, it is intended here that the two electrodes and the interconnect form the reference in deconvoluting the overall degradation of SOC performance.

In the sections that follow, the fundamental processes and presumed degradation mechanisms characterizing these components will be discussed. Before that, the importance of microstructural representation will be explained, as a key to the correct interpretation of observed degradation phenomena in each component afterward.

2.1 | Microstructural representation of SOC electrodes

Many works in the literature focus on the phenomena at the microscale level, in particular within the electrodes (positive and negative).⁴⁹ The reason is that microstructural analysis can determine the behavior of the triple-phase boundaries (TPBs), which govern the number of electrocatalytic sites available for reaction and their accessibility by the transport of reactants and products.

Several studies concern improvements in TPB characterization by non-destructive 3D imaging and the corresponding modeling approaches for the evaluation of TPB loss over time during operation. In principle, continuous models consider homogenized electrode properties that can be computed based on real 3D reconstructions.⁵⁰ A new method has been introduced for analyzing the pathway properties of each TPB site in the electrode structure based on 3D image data in ref. 51, where two new site-specific parameters describing the quality of the TPBs are defined:

Total triple-phase boundary (TPB) density

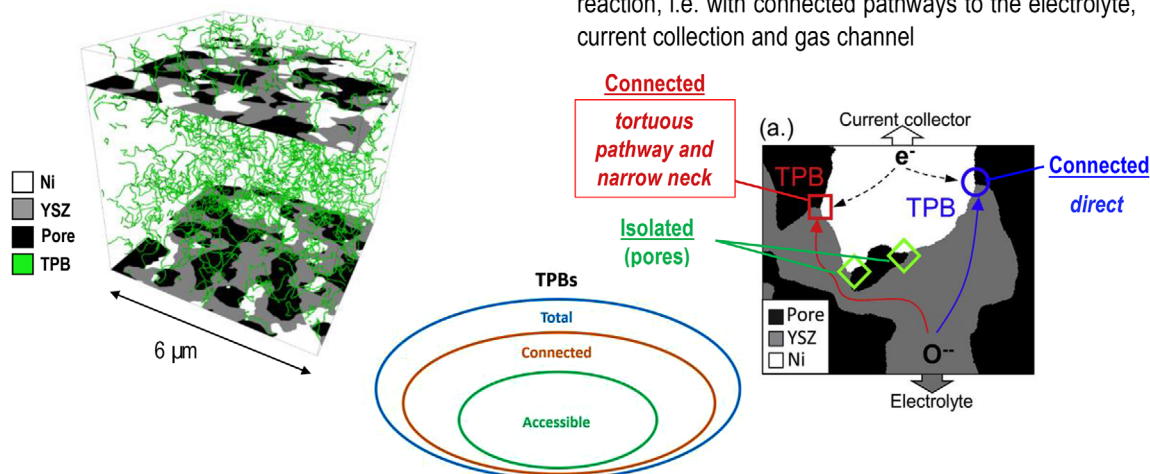


FIGURE 4 Accessible TPB for the electrochemical reaction as the active subset of connected and total TPB in a Ni-YSZ porous structure⁵²

(i) the TPB tortuosity that seeks to quantify the distance from the TPB sites to the source/destination through each phase and (ii) the TPB critical pathway thickness that seeks to quantify the bottleneck width of the pathways to the TPB sites. The new approach is experimentally tested on composite electrodes, Ni-YSZ and LSCF-GDC, and provides valuable microstructural insight.

Further advancement in the 3D discrete representation of the heterogeneous structure is developed in ref. 52, based on the so-called electrochemical “fin” model. It is applied to a 3D discrete representation of the heterogeneous structure provided by skeleton-based partitioning. The results on real and artificial structures show (see Figure 4) that the 3D electrode microstructure is complex, the accessible TPBs are not uniform, the pattern varies depending upon the structure, and connected TPBs can be passivated. In both SOFC and SOEC electrode materials, the combined accessible TPB is mostly affected by each phase separately and the total accessible TPB is largely dominated by the ion-conducting phase. This capability to accurately quantify deviations from the ideal case is of relevance for the design of heterogeneous materials. From this point of view, it can be useful to have the possibility of generating representative digital twins of the real electrodes.^{53–59}

In a further step forward, laboratory-based X-ray micro-computed tomography has been developed to allow 4D (3 spatial dimensions plus time) studies without the destruction of the samples or the need to access synchrotron facilities.⁶⁰ The technique has been applied to study the effects of thermal cycling on the negative electrode structure with sub-micron resolution as well as on the change in interfacial contact between the negative electrode and electrolyte. It is shown that nickel sintering is minor during

Connected TPBs: subset available for electrochemical reaction, i.e. with connected pathways to the electrolyte, current collection and gas channel

start-up and shut-down compared to the long-term operation even at ramp rates of 3 K/min. Both sintering and loss of percolation were correlated to the triple-phase boundary losses but for operational thermal cycling with minor dwell times, the particle-particle loss of connectivity is the prominent mechanism.

A theoretical model applied to LSM-YSZ positive electrodes and Ni-YSZ negative electrodes in SOFC for the evaluation of the performance of an electrode formed by a mixture of electronic conductor/ionic conductor particles having a high a/d ratio is presented in refs. 23 and 61. A comparison with literature-sourced experimental data shows good agreement. The results of the model show that the effects of morphology, that is, the volumetric composition of the electrode and the dimensions of the particles strongly influence the electrode resistance. The reciprocal electrode resistance reaches a maximum in correspondence with a composition near the percolation threshold of the electronically conducting phase. The results stress the importance of obtaining good experimental data of percolation thresholds as well as a better theoretical insight into the critical percolation zones.

2.2 | Negative (fuel) electrode

The SOFC negative electrode (anode in SOFC-mode and cathode in SOEC-mode) should combine multiple functions, which sometimes oblige contradictory requirements. It should have both high catalytic activity and suitable electronic conductivity, good ionic conductivity together with appropriate porosity. Furthermore, it should be chemically and thermally stable in the operating

atmospheres and temperatures, possess good mechanical strength and compatibility with the materials as well as redox stability.

SOC negative electrode materials were initially developed for fuel cell operation and have been used in the reversed, electrolysis mode as well. Although the cell is identical, higher degradation is measured in electrolysis mode than in fuel cell mode. Degradation mechanisms of SOCs in both SOFC and SOEC mode have been largely discussed and reviewed especially for fuel electrode-supported cells,^{37,62–67} while very few reports can be found on post-test analyses of electrolyte-supported cells.^{68,69}

2.2.1 | Negative electrode composition

The negative electrode is a cermet made of a nickel catalyst and YSZ (or GDC) that benefits from good electrochemical performance, low price, and provides good compatibility with the ceramic electrolyte material. The slurry of NiO and the electrolyte is typically deposited (by screen printing or other methods) to achieve an electrode thickness of about 15 μm . Depending on the cell architecture, this active layer is either supported by the electrolyte (electrolyte-supported cell, ESC) or by a thick and porous layer of the cermet, the electrode itself (usually referred to as an anode-supported cell, ASC, meaning the negative electrode). In the cermet structure, metallic nickel particles are interconnected to conduct the electrons in the porous skeleton of the electrolyte ceramic material. The latter provides ionic conductivity and sites for the electrochemical reaction, and inhibits the coarsening of Ni particles during cell manufacturing and operation.

The most common materials for negative electrodes are Ni-YSZ or Ni-gadolinia- (or samaria-) doped ceria (Ni-GDC or Ni-SDC).^{70,71} Other materials have been investigated for steam electrolysis like lanthanum-substituted strontium titanate/ceria composites and perovskite materials.⁶⁵ A summary of the currently investigated fuel electrode materials can be found in the review.⁷² However, the most utilized material for negative electrodes is Ni-YSZ, and voluminous literature is available on this material in both SOFC and SOEC operation.

After the manufacturing process, where the YSZ/Ni ratio, pore formation, particle size, and sintering temperature are carefully controlled, the negative electrode cermet Ni-YSZ contains nickel in the oxide form (with its typical green color). In pre-operation conditions, the electrode is first reduced to form the Ni network, which changes overall mass, volume, composition, and porosity. This process is important for the negative electrode durability as it shapes the final Ni-YSZ composition and the microstructure

before operating the SOC.^{73–77} The relation between the initial powders and the microstructure of the pristine sample has to be considered to understand the degradation rate under operation. The most relevant parameters are the initial reduction temperature, operating conditions such as fuel utilization (SOFC)/steam conversion (SOEC), temperature, and so on.^{78–83}

2.2.2 | Negative electrode fundamental mechanisms

For a typical Ni-YSZ electrode, many reaction pathways have been proposed depending on the nature of the charge transfer across the Ni-YSZ interface. Among the different investigated scenarios, the most relevant phenomena correspond to a charge transfer based on an interstitial process,⁸⁴ and an oxygen⁸⁵ or hydrogen “spillover” mechanism.⁸⁶ The “spillover” mechanism corresponds to the surface reaction of charge transfer across the Ni/YSZ at the TPBs.⁸⁷ For instance, the oxygen adatom on Ni is reduced to form an oxide ion attached on the surface of YSZ (according to the reaction: $O_{Ni} + s_{YSZ} + 2e^-_{Ni} \leftrightarrow O_{YSZ}^{2-} + s_{Ni}$).

It has been shown by comparing simulations and experimental data that the hydrogen “spillover” would be the most relevant mechanism for the Ni-YSZ electrode,^{87–89} even if some recent studies have suggested that the oxygen “spillover” charge transfer could also be involved in the electrode response.^{90,91} A critical review of existing models concerning the $\text{H}_2/\text{H}_2\text{O}/\text{Ni}/\text{YSZ}$ electrode kinetics is presented in ref. 92. The use of limited sets of data to verify a given model is also discussed as well as the strengths of the models.

2.2.3 | The fate of nickel in the electrode microstructure: Coarsening and migration

The main source of degradation of an electrode-supported SOC during operation in both SOFC and SOEC modes concerns microstructural changes in the Ni network, due to both Ni migration and coarsening of Ni particles, which decreases the total TPB length.^{62,63,93,94} In ref. 95, a two-particle model for degradation analysis of Ni-YSZ cermet in SOFCs is proposed based on two main assumptions: (i) the difference in metal particle diameter is accepted as the driving force for the observed coarsening during long-term annealing, and (ii) surface diffusion of metal atoms on the particle surface is considered the dominant diffusion mechanism, since results showed that the proposed mechanism is fast enough to explain the recorded amount of Ni agglomeration in SOFC.

In recent years, advances in image processing and technologies allow probing the degradation mechanism down to micro- and nano-scale level. The degradation phenomena in Ni-cermet samples have been evaluated experimentally with resistivity measurements during 3000 h at 700 °C and 800 °C in 80 vol.% H₂O and 20 vol.% H₂. In ref. 96, the observed increase in the ohmic resistivity with time was related to the change in microstructure, estimated by image processing and X-ray fluorescence (XRF) analysis on virgin samples and samples exposed for 300, 1000, and 3000 h. The 3D microstructure, reconstructed using original spheres packing algorithms, suggests two processes leading to the Ni-YSZ degradation: Ni-phase particle coarsening and Ni migration and volatilization. Another example is the negative electrode micro-sample preparation and observation with transmission X-ray microscopy (TXM), which shows the microstructural evolution of the negative electrode with aging time.⁹⁷ The proposed 3D measurement directly shows the changes occurring in the same region of a negative electrode, enabling a new understanding of evolutionary processes. This technique has been applied to a Ni-YSZ sample aged at 1050 °C for 24 h and 48 h, in a 5% H₂/3% H₂O (Ar balance) gas mixture similar to typical fuel gas for SOFC. The high-temperature (accelerated) aging for 48 h at 1050 °C yields substantial structural changes in the Ni, YSZ, and pore networks, including coalescence of Ni particles, leading to a threefold decrease in overall TPB length. Nanoscale XRF spectroscopy has also been applied to acquire spatially resolved 2D element maps of long-term operated SOECs. For an electrode-supported cell, the concentration of nickel in the Ni-YSZ was evenly distributed in the pristine cell while after 6100 h operation without incidents, the presence of Ni at the negative electrode/electrolyte interface is significantly reduced with an inhomogeneous distribution at 6 μm from this interface to the outer surface of the electrode.⁹⁸ This observation is in line with a previous work⁹⁹ that shows that even after the apparent microstructural stabilization (of the averaged properties) after a few thousand hours, local morphological evolutions continue, thus hindering TPB accessibility by electrons and ions. Using synchrotron radiation, microstructural changes have been analyzed in the composite electrode of Ni-YSZ by X-ray nanotomography.⁵⁴ It has been shown that Ni coarsening induces a significant decrease in both the density of TPB and the Ni/gas specific surface area. Furthermore, the Ni coarsening rate is independent of the electrode polarization and the Ni sintering is inhibited by the YSZ backbone.

Percolation of the Ni particles provides the needed electronic conductivity, which, through Ni migration, is disrupted and leads to an increase of the ohmic resistance. The low accelerating voltage scanning electron microscope (SEM) mode allows for visualizing and quantifying the

degree of Ni percolation.¹⁰⁰ The decrease of the percolation can be clearly correlated to an increase in degradation, specifically an increase of the ohmic resistance of cells operated in fuel cell mode,¹⁰¹ in steam electrolysis mode,¹⁰² and in co-electrolysis mode.¹⁰³ Beyond the density of TPB and their accessibility by the transport of gas species, electrons, and ions, Rinaldi et al.¹⁰⁴ have investigated the additional potential effect of local morphology (so-called “available length”) near the TPBs. A spilling algorithm was developed in this context to characterize the surfaces available for diffusion at TPBs. A strong correlation between the available length and the extension of TPB lines is observed for Ni but not for YSZ, despite the predominance of convex shapes, which likely originate from the Ni reduction. This suggests possibilities for controlling the available length by the manufacturing route, depending specifically on the electrocatalytic properties of the phases in composite materials.

Testing of cells in SOEC demonstrates the importance of the sealing material on the negative electrode, which may prevent initial passivation in the first few hundred hours of electrolysis.¹⁰⁵ The degradation analyzed by EIS is found mainly to be caused by increasing polarization resistance associated with the Ni-YSZ electrode (cell voltage degradation of 2%/1000h). Post mortem analysis showed the accumulation of impurities in the negative electrode and microstructural changes at the electrode-electrolyte interface. In the frame of FCH JU-funded projects ENDURANCE and SOPHIA, a detailed study of negative electrode degradation is performed on cell and stack levels. Comparative long-term tests are carried out in SOFC and SOEC modes on SOLIDpower cells.^{53,54,58}

Regarding Ni agglomeration in the bulk of the electrode, it has been shown that Ni coarsening is thermally activated and independent of electrode polarization in SOFC or SOEC mode.^{54,106} Besides, it has been found that the steam content in the gas flow accelerates the rate of Ni coarsening.^{107–109} Moreover, it has been shown that the YSZ backbone could play a crucial role by stabilizing the cermet microstructure and thus preventing massive Ni coarsening in operation.^{54,110–112} This inhibiting effect of the YSZ network on Ni coarsening has been ascribed to the interfacial bonding property of this ceramic-metal interface.^{113–115} As a result, it has been found that Ni particle growth tends to slow down over time.¹⁰⁷ Nevertheless, since the agglomeration induces a significant drop in the density of TPB lengths, it has been estimated using a multiscale modeling approach that the microstructural change in the cermet could explain around 25–30% of the total cell degradation at 850 °C after 1000–2000 h of operation.⁵⁴ This result is in good agreement with the study of Faes et al.⁹⁴ who have found that Ni-YSZ electrode degradation occurs principally during the first 500 operating hours. For stack

tests carried out over more than 1000 h, the degradation of Ni-YSZ is responsible for 18–41% of the total degradation depending on the initial microstructure.

It is nowadays clearly established that the mechanism of Ni coarsening corresponds to the local sintering of adjacent particles driven by the minimization of the Ni-specific surface area by the growth of the biggest particles to the detriment of the smallest ones.^{54,95,107,116} In this context, as already mentioned, it is suspected that Ni adhesion on YSZ can slow down the process by anchoring the metallic particles onto the ceramic backbone. Surface diffusion of Ni atoms or Ni(OH)_x species seems to be the privileged mass transfer phenomenon^{108,116–118} even if transport in the gas phase as Ni(OH)₂ species or by solid-state diffusion of vacancies is also possible.^{116,119,120} For both cases, the mechanism is thermally activated and sensitive to the steam content in the gas phase, explaining the role of temperature and the effect of water content on the agglomeration rate. Based on a local coarsening process, Ni particle growth has been successfully reproduced using models for the sintering of two particles such as the classical power-law equation.^{95,120–123} In this case, a rather high exponent on the Ni particle diameter was obtained by fitting the experimental data ($n \approx 8$).^{54,93} It can be noticed that these values reflect the inhibiting role of the YSZ network on the Ni agglomeration but they would be consistent with a surface diffusional mechanism. Finally, it has been shown that phase-field modeling can constitute a powerful tool to accurately simulate Ni agglomeration in the complex 3D microstructure of the cermet since the process is based on the minimization of the Ni/gas surface energy.^{116,124,125}

In contrast with the agglomeration controlled by a local sintering process, migration over long distances can change the Ni distribution within the electrode. Post-test characterization has revealed that the process leads to Ni depletion only in the electrochemically active region of the cermet and is strongly promoted under electrolysis conditions.^{37,106,126} Based on these observations, it has been suggested that the migration must be driven by the local cathodic overpotentials in the functional layer.^{93,127,128} Besides, it is suspected that the steam content in the gas stream could accelerate the process. It has been also shown that the rate of Ni migration is dependent on the initial cermet microstructure.¹²⁹ Therefore, the migration can result, in case of a coarse cermet microstructure, in complete disappearance of Ni in the active functional layer. The impact of the Ni loss at the electrolyte interface has been estimated by a modeling approach in ref. 93. There it was shown that Ni migration must explain a significant part of the higher degradation rates measured in SOEC compared to the SOFC mode. Moreover, the full depletion of Ni from the functional layer, resulting in a thin layer of porous YSZ only, should explain in part the increase of the pure ohmic

resistance classically observed for cells tested in electrolysis conditions.

The exact underlying mechanism for Ni migration is still unclear. Different hypotheses have been proposed to account for the effect of electrode polarization on migration. Among them, Trini et al.¹⁰⁶ have suggested that migration could be driven by the gradient in Ni wettability properties depending on the local oxygen partial pressure controlled by the electrode overpotential, similar as to what was shown by Rinaldi et al.,¹³⁰ Monaco et al.,⁹³ and Nakajo et al.¹²⁸

Monaco et al.⁹³ have proposed that the process could be triggered by a deterioration of the Ni/YSZ interface due to an accumulation of oxygen vacancies in the double layer under cathodic polarization. This accumulation leads to decreasing bond strength at the ceramic-metal interface and thus to decreasing Ni wettability onto YSZ (by decreasing the work of separation or adhesion).^{114,131} Therefore, in this hypothesis, the migration would be driven by the change in Ni wettability, which is controlled by the evolution of the double layer as a function of the overpotential. This mechanism is also proposed and detailed in ref. 128. Indeed, they suggested the process could be ascribed to an evolution of the cermet morphology near the TPBs, induced by a change of the capacitance of the double layer in cathodic polarization. Despite all these studies, further investigations are still needed for a precise understanding of the mechanism controlling Ni migration.

2.2.4 | Nickel reoxidation

The microstructural changes that take place in the case of redox cycling are a severe cause of Ni-YSZ cermet degradation in terms of both electrochemical and mechanical performance.¹³² Although reoxidation should not occur under well-controlled working conditions, during long-term operation it is an expected, but unpredictable, phenomenon due to changes in the local conditions (leakage, fuel starvation, increased oxygen partial pressure, accidental switch off, and so on). The repetitive changes of Ni volume are the main cause of this degradation process that damages the YSZ network,¹³³ including the electrode/electrolyte interface, and reduces TPB density because of accelerated Ni coarsening. A comprehensive quantification of redox cycling can be achieved by coupling 3D tomography, real-time impedance spectroscopy, and mechanical analysis.^{94,134} The unpredictable and high levels of degradation are probably the reason for the intensive studies of Ni redox cycling and the efforts to find a preventing strategy.

In the case of negative electrode-supported cells, the mechanical stability of the Ni-YSZ support is the most

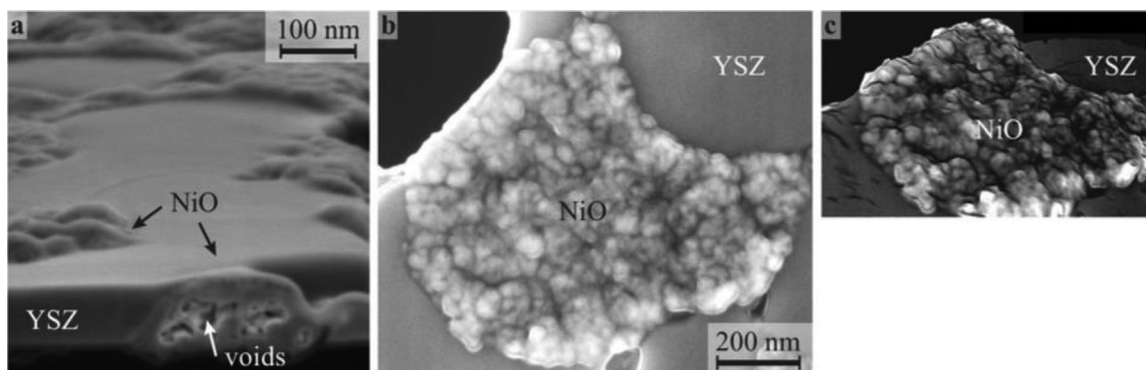


FIGURE 5 (a) SEM image of a cross-section milled by FIB highlighting internal pores created during oxidation and expansion out of the specimen plane, (b) SEM secondary electron image, and (c) corresponding three-dimensional reconstruction of the topography of a NiO grain (stereoscopic image)⁷⁸

critical element determining the cell failure.^{135,44,110,136} Owing to the Ni plasticity, creep during operation can somewhat compensate for this vulnerability.^{137–139}

The dependence of the overpotential on both electrical and ionic conductivity through the cermet electrode has been assessed by Kirtley et al.¹⁴⁰ by monitoring the NiO growth in fuel cell mode at constant load operating conditions and elimination of the fuel flow with in situ vibrational Raman scattering and by comparing the rate of NiO growth to the cell overpotential and EIS data.

The reduction/oxidation kinetics on Ni-YSZ cermet have been studied on dense (no open porosity) two-phase NiO+YSZ samples, with and without additives (CaO, MgO, TiO₂), that were reduced in a hydrogen-containing environment.¹⁴¹ A theoretical model based on two in-series kinetic steps – diffusion and interface reaction – indicates that the reduction kinetics are linear (interface-controlled) and thermally activated while the reoxidation kinetics are nearly parabolic (diffusion-controlled) and essentially independent of temperature. The interface control of the reduction process implies that gas-phase diffusion through porous Ni+YSZ, formed upon reduction of NiO to Ni, is considerably faster than the kinetics of the actual reduction reaction occurring at the interface separating the pristine and the reduced regions. In contrast, the diffusion control of the reoxidation process is attributed to slow, gaseous diffusion considering the very small amount of porosity remaining during the reoxidation of Ni to NiO.

Faes et al.¹⁴³ and Jeangros et al.^{79,142} explained the reduction and oxidation kinetics of Ni(O) particles as well as of Ni(O)-YSZ cermet through a series of detailed, systematic and related energy-filtered TEM (ETEM) studies (see Figure 5). Using ETEM on a sequence of images as a function of temperature, the speed of progression of the NiO-YSZ reduction reaction front in all three dimensions was obtained, providing a 3D monitoring

of the reaction. During Ni reoxidation, the creation of a porous structure, due to mass transport, accounts for the redox instability of the Ni-YSZ electrode. The expansion of NiO during a redox cycle and the presence of stress in YSZ grains could be directly observed. For NiO-YSZ samples, the transfer of oxygen from NiO to YSZ triggers the reduction reaction. The symmetry of Ni-NiO grain boundaries during reduction was found to play a role: automated crystal orientation ETEM mapping revealed that coherent NiO twin boundaries remain intact during reduction, while NiO grains separate by an incoherent boundary detachment from each other when reducing to Ni, affecting the Ni phase percolation.

In Laurencin et al.,¹⁴⁴ the oxidation kinetics and the cermet expansion were measured at different temperatures using a typical cermet substrate. Below around 750°C, the oxidation kinetics data were successfully fitted by a parabolic law with an activation energy of 118 kJ/mol, whereas the oxidation was not thermally activated at higher temperatures. This transition indicates a modification of the oxidation mechanism. At high temperature, the kinetic rate of the Ni oxidation is sufficiently high and the process is limited by the gas diffusion across the thick porous cermet. Conversely, when decreasing the temperature, the thermally activated kinetic constant for the Ni oxidation becomes sufficiently low so that the mechanism is controlled by the oxidation of each Ni particle in the cermet, was consistent with the results of SEM and local X-ray μ -diffraction characterizations (homogeneous re-oxidation in the cermet thickness at low temperatures, at higher temperature a Ni/NiO gradient in the cermet). These results were also found to be in good agreement with other studies devoted to the reoxidation of thick cermet supports.^{112,145,146}

Characterization of cracks after reoxidation using non-destructive 3D imaging based on X-ray nanotomography

has been carried out by Nakajo et al.⁹⁹ and Kiss et al.¹⁴⁷ on Ni-based electrodes for SOFC/SOEC samples. With a spatial resolution below 20 nm, microstructures of non-exposed samples were compared to samples exposed to air at 800°C for 45 min. The morphology of the Ni(O) phase is observed to be completely different after re-oxidation. The detrimental effects of the cracks on the effective 3D transport pathways in the Ni-YSZ electrode under polarization are investigated using a skeleton-based discrete representation of the imaged volume and an analytical electrochemical fin model. Topological properties, effective ionic conductivity, and polarization resistance are calculated before and after oxidation. The calculations show that cracks in the brittle YSZ phase increase the effective ionic resistivity and polarization resistance in the range of $25 \pm 9\%$ and $12 \pm 5\%$, respectively.

Another source for the oxidation of the Ni-YSZ electrode is the higher oxygen partial pressure $p(\text{O}_2)$ that can cause oxidation-induced Ni degradation. Kawasaki et al.⁸¹ investigated the cell performance at high fuel utilization in SOFC to simulate situations around the system downstream. When the $p(\text{O}_2)$ at the Ni-YSZ electrode was lower than the threshold for NiO/Ni, the cell performance was stable while the performance was unstable above the threshold $p(\text{O}_2)$ value due to oxidation of Ni to NiO.

Using a classical electrode-supported cell, the Ni reoxidation induced by fuel starvation was also studied in ref. 148. As mentioned previously, it was shown that when the cell voltage drops below the theoretical threshold for the NiO/Ni/Air system (0.67 V at 800°C), a thin layer of cermet is electrochemically re-oxidized. The repetition of the redox cycles was found to induce an increase in both the serial and polarization resistances of the EIS diagrams measured under hydrogen at OCV between two redox cycles. This revolution was explained by the growth of the NiO layer from the electrolyte interface leading to mechanical damage in the active functional layer of the cermet.

It is worth noting that re-oxidation is accompanied by a macroscopic dimensional expansion of the cermet, which has been measured by many authors as a function of temperature and oxygen partial pressure. After first reduction, Ni particles are round; after a RedOx cycle, the Ni particles include micro-porosities that are stable under humidified reducing atmosphere for >300 h. This volume expansion can affect the stress state in the cell and provoke degradation in the structure. For the electrode-supported cell configuration, the expansion of the substrate induces high tensile stresses in the thin electrolyte, which is liable to trigger its fracture.^{135,149} For example, channel cracking of the electrolyte has been detected for a critical degree of oxidation (0.21% to 0.16% strain limit) of the cermet ranging between 60–70% at 800°C.¹⁴⁸ In ref. 111, a re-oxidation

strain limit from 0.12 to 0.21% was determined based on finite element modeling and a failure statistics approach considering the RedOx temperature, number of cycles (reaching a maximum after 10 cycles), and sample size. A safe RedOx temperature (below which no protective gas is needed) of 550°C was calculated and validated on stacks, though it appears that cell corners undergo several cycles depending on stack design and fuel utilization. In refs. 150 and 151, a DoE approach, varying the NiO proportion (40–60 wt% of the ceramic powders), the pore-former proportion (0–30 wt% corresponding to 0–64 vol.%), the NiO particle size (0.5–8 μm), and 8YSZ particle size (0.6–9 μm) showed that expansion after re-oxidation is mostly influenced by the sample porosity whereas the NiO content, between 40 and 60 wt%, did not show any impact.

As opposed to the Ni electrode-supported cell, the electrolyte-supported cell design is much more tolerant regarding cermet reoxidation. Indeed, this structure can withstand several redox cycles with only mild deterioration of cell performance without catastrophic failure of the thick electrolyte.^{152,153}

A mitigation strategy has been proposed against the degradation caused by periodic extension/shrinkage, consisting of pre-oxidation treatment at 600°C.¹⁵⁴ This leads to an initial expulsion of some NiO particles at the outer electrode surface, ensuring more “free space” and thus increased tolerance toward further oxidation/reduction. The positive effect of preliminary oxidation/reduction is found also in ref. 155.

2.3 | Oxygen (positive) electrode

Materials and structure of the oxygen electrode are related to the oxide ion formation/consumption (SOFC/SOEC) and its transport. By these, the activity and the stability of the oxygen reduction reaction (ORR) or the oxygen evolution reaction (OER) are governed, and together with the tolerance towards contaminants (like chromium, sulfur, etc.) make up fundamental characteristics for the performance of the electrode.

2.3.1 | Oxygen electrode composition

Perovskite-type lanthanum strontium manganite (LSM) has been used for decades in SOFC operation because of its thermodynamic stability. Even though LSM possesses a high electronic conductivity, the active sites are limited due to the poor ionic conductivity of the material. Furthermore, it is known that LSM is not suitable as an oxygen electrode for SOEC due to various compositional

and microstructural instabilities under anodic current passage, such as deficiency of oxygen vacancies, intergranular fractures in the electrolyte, and catastrophic delamination failure of the electrode due to densification of LSM after long-term operation.¹⁵⁶ Hence, nowadays, mixed-ionic-electronic-conducting perovskite oxides are widely used as oxygen electrodes due to their high ionic and electronic conductivity as well as the large oxygen-surface exchange rate constant. The most popular and representative oxygen electrode material for SOFC and SOEC is lanthanum strontium cobalt ferrite (LSCF) perovskite.³²⁵ Mai et al.¹⁵⁷ made a comparison of the iron- and cobalt-containing perovskites as oxygen electrode in SOFC mode with the manganite-based perovskites to assess the properties and the performance of the LSCF electrode. Other types of structures like Ruddlesden-Popper or double perovskite oxides are also considered because of their stability under the oxidizing atmosphere in SOEC mode. Perovskite-based materials used for oxygen electrodes have been reviewed in ref. 72. The engineering of the composite oxygen electrode is of importance and numerical analysis allows optimizing the different parameters as shown in the study by Zheng et al.¹⁵⁸ Thanks to this paper, a relation between porosity, current collector thickness, and interconnect coverage has been demonstrated as well as the need for interrelated optimization since changes in one of the microstructural or geometrical parameters affect the transport of oxide ions, and electrons, i.e., all aspects of the coupled reaction-transport processes should be considered for optimization of the oxygen electrode. It was pointed out that LSCF reacts with the electrolyte material YSZ at sintering temperature imposing to add a diffusion barrier made of gadolinia-doped ceria ($\text{Ce}_{0.9}\text{Gd}_{0.1}\text{O}_{1.95}$ labeled as GDC or $\text{Ce}_{0.8}\text{Sm}_{0.2}\text{O}_{1.9}$ SDC) between the YSZ electrolyte and the oxygen electrode.

Rare-earth nickelates $\text{Ln}_2\text{NiO}_{4+\delta}$ ($\text{Ln} = \text{La}, \text{Pr}, \text{Nd}$) are also promising alternative materials developed for the oxygen electrode.^{159–162} These compounds belong to the Ruddlesden-Popper RP series with general formulation $\text{A}_{n+1}\text{M}_n\text{O}_{3n+1}$. Their structure can be described by the intergrowth of octahedra layers (perovskite-type) with AO blocks (NaCl-type). In this formulation, the subscript n is related to the number of octahedra layers with $n = 1$ for $\text{Ln}_2\text{NiO}_{4+\delta}$. Depending on n and A , these oxides can exhibit either an under- or an over-oxygen stoichiometry (δ), resulting in mixed electronic and ionic conductivities. Among the $\text{Ln}_2\text{NiO}_{4+\delta}$ compounds, which exhibit an oxygen over-stoichiometry, several studies have been devoted to the solid solution of lanthanum-praseodymium nickelate, $\text{La}_{2-x}\text{Pr}_x\text{NiO}_{4+\delta}$ ($0 \leq x \leq 2$)¹⁶³. It has been shown that these compounds have good properties in terms of ionic conductivity and oxygen exchange even at low temperature (600–700°C).^{164,165}

2.3.2 | Oxygen electrode fundamental mechanisms

Despite the number of investigations, the complex, multi-step ORR continues to be an active research field, since the cathodic performance in SOFC contributes significantly to the polarization losses. For the porous O_2 electrodes classically made of mixed conductors such as LSCF,¹⁶⁶ have developed the “ALS” analytical model in which the electrode response is dominated by a “bulk path” taking into account the oxygen vacancies solid-state diffusion in LSCF and a global reaction of oxygen exchange on the surface. Many studies have clearly stated that this mechanism allows predicting accurately the electrode response at OCV and under cathodic polarization.^{167,168} However, it has been recently shown for LSCF that a change of reaction pathway arises at low anodic current with a transition toward a “surface path” controlled by the change transfer at TPBs.^{169,170} For composite electrodes made of LSCF and GDC, this last mechanism becomes the prevalent pathway whatever the operating mode, since, for this particular case, the electrode presents a high density of TPBs.¹⁷¹ Despite all these efforts, there is still a need for more sophisticated models that can describe the integrated degradation picture.

2.3.3 | Major degradation sources in the oxygen electrode

Recent experimental studies have reported that the degradation of the oxygen electrodes made of under-stoichiometric materials such as LSCF or lanthanum strontium cobaltite (LSC) is significantly accelerated in SOEC compared to SOFC mode.^{18,172,173} The presence of water vapor in the air flow accelerates degradation,^{174,175} while the precise role of operating temperature remains unclear.^{176,177} The underlying mechanisms of material deterioration are not completely understood yet, though the major degradation sources reported within the oxygen electrode are cation inter-diffusion (i.e., Sr diffusion) between the cell components and formation of secondary insulating phases,³⁷ poisoning with contaminants (CO_2 , H_2O , Cr, S, Si)^{7,178,179,180–181,182} and delamination. The electrode microstructure, the cell manufacturing conditions, or even the geometrical configuration could play a key role in LSCF or LSC stability.

It has been found by 3D electrode reconstruction that the LSCF microstructure is stable and does not evolve significantly upon operation.^{183–185} However, Sr diffusion and the formation of SrZrO_3 at the electrode/electrolyte interface is reported^{37,186} when Sr-containing electrodes are used as an oxygen electrode. LSCF oxygen electrodes

sintered at 1050°C for 2 h and tested for 500 h at 750°C/0.7 V showed substantial degradation. Using SEM, no significant microstructural changes were observed. By applying X-ray photoelectron spectroscopy, a significant Sr enrichment at both LSCF-SDC and LSCF-Au interfaces was highlighted that could account for the substantial increases in both ohmic and non-ohmic resistances observed during the test. It has been shown using X-ray diffraction that the structure of an LSCF positive electrode ($\text{La}_{0.6}\text{Sr}_{0.4}\text{Co}_{0.2}\text{Fe}_{0.8}\text{O}_{3-\delta}$) was gradually changing over the course of more than 60 h of operation in air under typical SOFC operating conditions.¹⁸⁷ As these materials are known to react with YSZ forming a SrZrO_3 secondary phase, a doped ceria (GDC or SDC) barrier layer is usually added between the electrode and the electrolyte. The densification as well as the thickness of the ceria barrier layer are two crucial parameters to limit the diffusion of Sr and mitigate the reactivity with YSZ. However, it is difficult to densify GDC or SDC layers prepared by conventional ceramic processing techniques because the sintering temperature of the barrier layer is restricted to below 1250°C, above which harmful chemical reactions with the underlying YSZ electrolyte can take place. The universal approach to address this issue is to employ sintering aids to enhance the densification of the barrier layer.^{188–190} However, simply promoting the intrinsic sintering behavior of the barrier layer by employing sintering aids induces other harmful secondary reactions with the adjacent electrolyte during the multilayer fabrication process.¹⁹¹ Moreover, the rapid shrinkage of the film caused by the action of sintering aids results in differential densification and poor adhesion with the electrolyte, generating various processing flaws and delamination cracks¹⁸⁸. Recently, in ref. 192, a highly reliable barrier layer is constructed via a two-layer approach, in which the top and bottom layers perform individual functions to precisely control the bulk and interfacial properties using specially designed nanoparticles in the top and bottom layers.

Another approach is to use physical vapor deposition (PVD) to get dense a barrier layer without sintering. It has been shown that dense PVD coating is a more efficient barrier layer than porous screen-printed GDC when the cell operates in SOFC mode.^{193,194} The cation diffusion behavior in an LSCF/GDC/YSZ system was investigated under cathodic polarization where the dense GDC interlayer, about 1 μm in thickness and a columnar structure, was prepared by pulsed laser deposition (PLD). The results indicate that under polarization, the formation of SrZrO_3 along both LSCF/GDC and GDC/YSZ interfaces was accelerated by an inter-diffusion of Sr and Zr via grain-boundaries of columnar GDC.¹⁹⁵

It has been observed that such an inter-diffusion of chemical elements in YSZ and GDC or even

the precipitation of SrZrO_3 can occur during cell manufacturing.^{98,196,197} The GDC sintering temperature is a key factor controlling the reactivity and the extent of the inter-diffusion of Sr, Gd, and Zr for the pristine cells.¹⁹⁸ In ref. 199, the degradation phenomena were investigated at 780°C for a stack tested 3000 h in SOFC mode. Post mortem comparative analysis with pristine cell performed by XRD, Raman spectroscopy, SEM with wavelength-dispersive X-ray spectroscopy (SEM-WDX), and scanning transmission microscopy with EDX (STEM-EDX) have revealed that diffusion takes place at the barrier layer/electrode interface and the barrier layer/electrolyte interface where insulating phases and solid solutions have been registered at both interfaces in both the pristine and the tested cell. This result illustrates and confirms the importance of the preparation stage. In a further study using Raman spectroscopy and imaging techniques, cation diffusion was evidenced during the fabrication process.¹²⁷ These results are consistent with the results of Matsui et al.¹⁹⁶ who have shown that the migration of Gd in YSZ and the dissolution of Zr in the barrier layer can be prolonged upon operation resulting in a reduction of the ionic conductivities of the affected layers. Thus, an optimum temperature has been proposed for the fabrication of the GDC barrier layer, as a balance between the densification of GDC and suppression of the inter-diffusion of Sr, Gd, and Zr.²⁰⁰ In contrast, the performance and durability of LSCF-SDC composite oxygen electrode have been improved greatly by the use of a dense and uniform SDC barrier layer prepared by coating cerium and samarium octoates, followed by sintering at 1050°C.²⁰¹ Besides a remarkable suppression of SrZrO_3 formation for 5500 h in the AST at 900°C for both operation modes in a symmetrical cell,²⁰² the effect of the uniform barrier layer on the electrode performance has been clarified.

It is worth mentioning that precipitation of Sr-O type secondary phase at the LSCF surface leads to form a passivating film blocking the surface reactions for the electrochemistry.^{186,203,204} Such a diffusion was observed in SOEC operation mode with material transport into the ceria-based barrier layer and compositional variations in the sub- μm range in the oxygen electrode.²⁰⁵ Oxygen electrodes operated for different hours were analyzed ex-situ using Mössbauer spectroscopy, XRD, and classical imaging techniques (SEM and TEM).²⁰⁶ XRD and TEM revealed the appearance of Co_3O_4 during the SOEC operation and SEM analyses confirmed the formation of SrZrO_3 at the electrode/electrolyte interface. The spectral analysis confirmed the reduction of iron from Fe(IV) to Fe(III) in LSCF after long-term operation. The fraction of Fe(IV) in the electrode decreased with time and 18%, 15%, 13%, and 11% were obtained for 0, 1774, 6100, and 9000 h of operation, respectively.

In addition, symmetrical cells were tested with two types of LSCF electrode microstructures. The LSCF microstructural properties are quantified in a 3-D volume and used as input data in a dynamic micro-scale electrochemical model, which describes the relation between the microstructure and the impedance response. The numerical tool includes two parallel reaction pathways with an oxygen exchange at the LSCF/gas surface and a charge transfer at the TPB. Electrochemical Impedances are computed in the time domain at OCV, as well as under anodic and cathodic polarizations. Simulations allow the microstructural parameters to be linked to the basic mechanisms of electrode operation according to the electrode polarization. The simulations show that the transition detected at low anodic polarization is due to a change in the dominant reaction mechanism passing from the bulk to the surface path. The relative contribution of the two pathways is also investigated as a function of temperature.^{170,207} In a further step down to the nanoscale, 2D maps of $54 \times 14 \mu\text{m}$ were acquired with XRF nano-imaging on long-term operated SOECs.⁹⁸ Such a technique provided clear experimental proof of the diffusion of the different elements. The spatially resolved technique allowed locating the different chemical elements and shows that the prepared cell architecture of an electrode-supported cell is rather LSCF/GDC/Gd/Sr/YSZ/Ni(YSZ) than LSCF/GDC/YSZ/Ni(YSZ) even before any electrochemical reaction. Sr diffuses through the GDC layer to form a dense layer of $\sim 0.7 \mu\text{m}$ at the GDC/electrolyte interface, which does not change significantly under polarization. In addition, Sr is only present at this interface and not in the GDC layer suggesting that there is no concentration gradient of Sr from the LSCF to the electrolyte.

Advanced characterization techniques using synchrotron radiation allow probing the oxygen electrode at the micro and nanoscale. X-ray microspectroscopy was used to study the interface between an SDC electrolyte and lanthanum ferrite oxygen electrodes ($\text{La}_{0.4}\text{Sr}_{0.6}\text{Fe}_{0.8}\text{Cu}_{0.2}\text{O}_3$ [LSFCu]; $\text{La}_{0.9}\text{Sr}_{0.1}\text{Fe}_{0.85}\text{Co}_{0.15}\text{O}_3$ [LSCF]), at a submicrometric level. It has been shown that in SDC–LSCF bilayers with prolonged thermal treatments at 1150°C the segregation of Sm and Fe occurs in micrometer-sized perovskite domains.²⁰⁸ A pristine LSCF oxygen electrode was studied using 2D and 3D X-ray μ -diffraction and μ -fluorescence that allowed a larger field of view in comparison to electron microscopy techniques. The formation of SrZrO_3 at the GDC/YSZ interface region was identified and micro SrZrO_3 inclusions were found in the $23 \mu\text{m}$ thick LSCF layer.²⁰⁹ Reconstruction with X-ray nanotomography was carried out on typical Ni-YSZ/YSZ/GDC/LSCF cells tested above 1000 h in fuel cell and electrolysis mode.

Using negative electrode-supported cells, it has been shown that the precipitation of zirconates related to LSCF decomposition is favored mainly during electrolysis operation and is limited during fuel cell operation.^{18,37,173} This can explain the higher degradation rates observed in SOEC compared to SOFC mode. On the other hand, for electrolyte-supported cells, Villanova et al.⁹⁸ have shown that cobalt is the most unstable element during the electrochemical reaction as it diffuses through the GDC barrier into the electrolyte.

For the interpretation of these results, a multi-scale model has been applied in ref. 18. The simulations have shown that electrolysis operation leads to a strong depletion of oxygen vacancies in the LSCF, while an increase is expected in fuel cell mode. Therefore, it has been proposed that the accumulation of the oxygen in the LSCF lattice under anodic current could trigger LSCF demixing inducing the segregation of the Sr^{2+} cations and the formation of strontium oxide (SrO) on the electrode surface. For instance, Oh et al.¹⁷⁶ detected by Auger and TEM the precipitation of a SrO based compound on the LSCF surface after aging at $600\text{--}900^\circ\text{C}$. In the second step, the SrO on the LSCF surface could be evaporated under hydroxyl volatile molecules²¹⁰ that can diffuse in the porosities of the electrode and the barrier layer to react with the electrolyte and form the zirconates.

Kim et al.²¹¹ have also suggested that the global kinetic constant of oxygen exchange (k_{chem}) could be affected by the stoichiometry change with Sr-deficiency on the “clean” part of the LSCF surface. As a consequence, Wang and Barnett²¹² have shown that the kinetic constant k_{chem} decreases after aging at $700\text{--}800^\circ\text{C}$ by an order of magnitude and they attributed this evolution to the passivation of the LSCF surface. Besides, the loss of Sr within the perovskite lattice results in a decrease of the oxygen chemical diffusivity or LSCF ionic conductivity.²¹³ Therefore, for aged LSCF at 800°C , Wang et al.¹⁸⁵ have used the “ALS” model to fit the evolution of the EIS diagrams and they have found that the degradation rate was mainly ascribed to the decrease of both the oxygen surface exchange rate and solid-state diffusion coefficient. For all these reasons, it is speculated that the demixing of the LSCF, which is favored under anodic current, could explain in part the higher degradation rates obtained in electrolysis conditions compared to fuel cell mode.

Nevertheless, the evolution of the inter-diffusion layer is still a subject of investigation, especially considering electrolysis operation. From this point of view, as pointed out in ref. 173, the development of alternative oxygen electrode materials has to be envisaged as a prerequisite for SOEC long-term operation.

The electrode performances are increased by increasing the content of praseodymium in $\text{La}_{2-x}\text{Pr}_x\text{NiO}_{4+\delta}$. However,

Pr-rich compounds present a chemical phase instability when exposed to high temperatures (the higher the Pr content, the larger the chemical instability). Indeed, the lanthanum-praseodymium nickelate is prone to decompose in high order secondary phases such as $\text{PrNiO}_{3-\delta}$, $\text{Pr}_4\text{Ni}_3\text{O}_{10+\delta}$, and Pr_6O_{11} .^{214–216} Nevertheless, most of the products resulting from the $\text{La}_{2-x}\text{Pr}_x\text{NiO}_{4+\delta}$ decomposition are also electrochemically active. For instance, it has been established that the Pr_6O_{11} praseodymium oxide is a very promising candidate exhibiting high performances when used as an oxygen electrode.^{217,218}

The durability behavior of the lanthanum-praseodymium nickelates is still unclear and remains nowadays a subject of investigation. No sign of reactivity with GDC has been detected after aging while the electrode decomposition is accelerated upon operation.^{216,219} It has been observed that the polarization resistance is not affected by operation under anodic polarization indicating that these materials could be envisaged as oxygen electrodes for electrolysis applications. On the contrary, high degradation rates have been measured in cathodic polarization. This behavior has been ascribed to a deterioration of the interface leading to delamination observed after testing at room temperature.¹⁵⁹ The underlying mechanism responsible for this degradation is not clearly understood yet. It could be ascribed to the over-stoichiometry decrease induced by the cathodic current leading to a high depletion of interstitial oxygen at the electrolyte interface. It had further been postulated that nickelate oxygen electrodes might be less prone to poisoning than the usual perovskites. However, studies^{220,221} have shown this not to be the case. Yokokawa et al. have studied the degradation mechanism due to air-side impurities within a series of NEDO projects.^{7,38,178,222,223} The 2015–2019 NEDO project highlighted the correlation between the oxygen electrode polarization and the ohmic losses. Detailed analysis of the oxygen electrode degradation finds in addition to the Cr poisoning a new degradation source – S poisoning coming from SO_2 contamination of the airflow.^{180,182} It is supposed that the degradation of LSCF is caused by reaction of the SrO component with the acidic gaseous species CrO_3 and SO_2 combined with the formation of $\text{Co}_2\text{Fe}_2\text{O}_4$ precipitates that leads to Sr, Co(Fe) depletion and incorporation of O^{2-} in the oxide ion vacancy sites bringing to electrochemical performance decrease. The detailed analysis reveals that there is a common degradation mechanism among the Sr volatilization and Cr and S poisoning. Cr poisoning is reviewed in Section 2.4.

Regarding sulfur poisoning, even very low concentrations of SO_2 in the air flow induces a substantial loss in electrode performances, which can constitute a non-negligible source of degradation at the stack level.^{224,225} Sulfur deposition in the electrode is increased with

decreasing operating temperature.²²⁶ The contamination is also activated under polarization in the electrode active region.^{224,227} It has been shown that electrode performance degradation is due to the decrease of the oxygen exchange kinetic constant k_{chem} that has been ascribed to the formation of SrSO_4 on the LSCF surface.²²⁸ From this point of view, the mechanism of sulfur poisoning would be linked to the Sr instability in the perovskite structure associated with the material phase decomposition^{226,229}.

In addition to the contaminants, important factors that govern cell performance with respect to the oxygen electrode are the operating temperature and polarization (SOCTESQA).^{28,223,230}

In ref. 222, the influence of operating temperature and gas conditions (presence of H_2O and CO_2) was studied for SOFC operation by EIS in three-electrode configuration to find corresponding degradation mechanisms. A correlation between the blocking effect of the contaminants and the operating temperature was found. A combination of long-term tests and postmortem analysis of experiments performed at different temperatures and current densities showed that oxygen electrode degradation in SOEC mode dominates at a higher current density and lower temperature.²⁸ Similar results were obtained for operation in humid air with LSM-YSZ composite oxygen electrodes in SOFCs.²³¹

2.4 | Interconnect

Even though interconnects have no active role in the electrochemical reaction, they constitute a critical component in SOC stacks considering the required properties and the operating conditions to which they are subjected.^{232–234} The interconnect acts as a physical barrier separating fuel and oxidant compartments avoiding mixing of reactants and has the primary functions of ensuring mechanical robustness of the entire stack assembly, providing uniform gas distribution over the electrodes and electrical continuity between adjacent cells. Considering the interconnect exposure to the SOC working temperatures and simultaneously to oxidizing and reducing atmospheres, material selection is demanding. Additionally, the direct contact with electrodes or current collectors introduces compatibility issues and further degradation sources.^{132,235}

To meet the abovementioned requirements, interconnect material should be characterized by (i) high electrical conductivity (maximum acceptable value of area-specific resistance, $0.1 \Omega\text{cm}^2$) to ensure an efficient electrical connection between cells and avoid the introduction of ohmic losses in the stack; (ii) good thermal conductivity (minimum value, $5\text{Wm}^{-1}\text{K}^{-1}$) to distribute the heat along the cell surfaces, mitigating gradients that could be

a source of thermal shocks for the ceramic components resulting in failure of the system; (iii) coefficient for thermal expansion (CTE) compatibility with adjoining materials (about $10.5 \times 10^{-6} \text{ K}^{-1}$ in the temperature range 25–900°C) to minimize the thermal stresses due to thermal cycles (start-up/shutting down or temperature changes during operation)¹³⁶; (iv) excellent chemical and corrosion stability in both oxidizing and reducing atmospheres, to preserve the electrical, thermal and mechanical properties for the whole stack lifetime. In addition to these characteristics, the interconnect should exhibit sufficient mechanical strength, minimal weight, and low materials and processing costs.^{236,237}

Thanks to significant progress made over the past years to reduce the SOC operational temperature to an intermediate-temperature (IT) range (600–750°C), conventional ferritic stainless steels (FSS) – characterized by a body-centered cubic structure ensuring CTE compatibility with the SOEC ceramic components – have become a popular choice for metallic interconnect (MIC) fabrication, as they provide the best compromise between the various above-mentioned requirements, particularly in the IT range. They also promote the formation of a protective chromia scale on the surface. FSS should contain a chromium amount within the range of 20–25 wt.% to ensure the formation of a continuous, protective Cr_2O_3 scale. Chromia exhibits a p-type semiconducting behavior in high oxygen partial pressure, thus decreasing its electrical resistance when increasing the temperature. This feature ensures a good conductivity at the operating temperatures.²³⁸

At operating conditions, in an oxidizing environment, the oxide scale on the interconnect tends to grow. The theory of high-temperature oxidation proposed by Wagner²³⁹ assumes that the diffusion of metallic cations from the substrate and oxide ions from the oxygen-rich atmosphere through the oxide scale takes place. Ions migrate through the lattice of the oxide scale by diffusion thus following a parabolic law. The parabolic rate constant relating the weight gain due to the scale growth to the oxidation time, provides an estimate of the high-temperature oxidation resistance of the material under investigation. For FSSs, K_p values are commonly in the range of 10^{-10} to $10^{-14} \text{ g}^2\text{cm}^{-4}\text{s}^{-1}$ and are strongly related to the operating temperature and chromium amount in the steel composition.^{42,240,241} There is also a report that the estimation of the K_p value is more complicated. The oxidation experiment of FSSs for longer times up to 500 h in ref. 242 shows a two-step thermal growth behavior due to a change in the growth rate of the chromia scale. In general, FSS is oxidized to form a twin-layer structured scale in which the MnCr-spinel oxide layer is formed on the chromia layer. Since the additional oxygen can pen-

etrate spinel oxide, the growth rate of the chromia scale increases abruptly after a certain annealing time. Nevertheless, the environmental and operating SOC conditions are much more aggressive than in common FSS applications, and the oxidation rates of FSSs are not acceptable for SOC application considering the target operating lifetime of the system. The excessive growth of the oxide scale leads to buckling and spallation phenomena, especially when the interconnect undergoes thermal cycles.²⁴³ Additionally, further oxidation of chromium contained in the scale to Cr(VI) volatile species lead to the pollution of the electrodes. This has led some manufacturers to develop specific FSS alloys like Crofer 22 APU/H or Sanergy HT, with higher Cr content and targeted microalloying composition for enhanced MIC performance. However, the cost of manufacturing these newly developed alloys is prohibitive, so that it has become common practice to employ conventional FSS alloys, like commercial K41/AISI441,²⁴⁴ protected by functional dense layers in the form of ceramic or metallic coatings.^{245–247} Bianco et al.²⁴⁸ performed ex-situ experimental benchmarking of more than 60 combinations of material solutions for SOFC interconnects, confirming that cheaper commercial stainless steel (K41) can compete with SOFC-specific steels. Moreover, it has been demonstrated that the application of protective coatings reduces the oxidation rate by two orders of magnitude, maintaining low ASR values.^{249–251} Furthermore, in-situ benchmarking on different solutions for AISI441/K41 MICs tested in SOFC stack operating conditions up to 10,000 h. Bianco et al.²⁵² revealed that physical vapor deposition (PVD) coating leads to the lowest voltage decay. It has also been demonstrated recently that steel nitriding decreases chromium evaporation with porous coatings.²⁵³

Degradation processes of either coated or uncoated FSS can be classified into two groups: those induced by interactions with gaseous agents (solid-gas reactions) and those induced by interactions at interfaces with active cells, sealing, or contact layer materials (solid-solid reactions). The most important degradation reactions occurring in steel MICs are summarized in Figure 6. Detailed discussion on MIC degradation mechanisms is not included here as many excellent review articles and book chapters on these topics can be found in the literature.^{9,232,237,254–256}

Lifetime prediction of coated and uncoated steel interconnects is a topic of paramount importance since the mechanical integrity of the entire SOC stack depends critically on interconnect durability. In general, the lifetime of materials in high-temperature environments remains very challenging to predict, since high-temperature components are often subjected to a complex combination of thermo-mechanical and oxidation-related damage mechanisms.^{48,136,139,257} Thus, for instance, wall thickness loss, scale spallation, and breakaway corrosion are

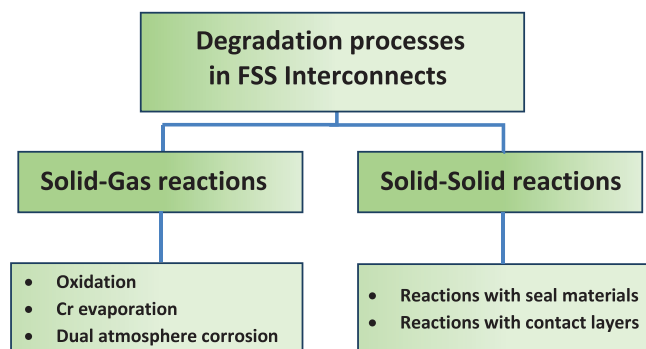


FIGURE 6 Breakdown of metallic interconnect degradation processes

the most frequently reported mechanisms causing high-temperature failure of components subjected to oxidation. Several studies report that oxidation degradation rather than intrinsic component thermo-mechanical properties are the predominant failure mode in thin chromia-forming steel MIC components.^{258,259} More specifically, according to these studies, the Cr reservoir in the bulk alloy may be considered as the primary lifetime-controlling factor on uncoated steels rather than the absolute Cr alloying concentration. The Cr reservoir model predicts that break-away corrosion is the most important failure-inducing oxidation effect and that oxidation-limited lifetime decreases with decreasing component thickness, as a more rapid consumption of the Cr reservoir by chromia scale growth and Cr evaporation takes place in the case of thinner MIC components. However, the interfacial properties between a coating layer and the steel substrate and the effect of sub-coating chromia scale growth have been successfully modeled for coated MIC lifetime prediction.²⁶⁰

The ability to rapidly form a protective and well-adherent chromia scale is at the basis of the well-known oxidation resistance of FSS alloys. However, chromia scales are not completely stable in the wet air conditions of SOFC cells due to the formation of harmful Cr volatile species in the form of CrO_3 and $\text{CrO}_2(\text{OH})_2$. Since the most active electrochemical areas of the oxygen electrodes, i.e. the TPB region, act as preferential nucleation sites for deposition of such volatile Cr species, this causes relevant oxygen reaction deactivation and overall cell performance degradation.^{261–263}

Additionally, Cr evaporation can have important consequences on MIC oxidation resistance, especially at lower operating temperatures. According to Trebbels and Asteman, continuous Cr evaporation at temperatures between 600 and 900°C will lead to the formation of progressively less protective oxide scales and eventually to destructive break-away oxidation as a result of fast-growing Fe-rich oxide formation.^{23,244,264–266}

Although the stress is on the electrodes and electrolytes, the sealant is also polluted which introduces other degradation sources. In ref. 267, the analysis of a sealant/interconnect from the inlet and outlet manifolds of a stack operated at 750°C for 4000 h shows that the sealant exposed to the outgoing air is significantly polluted by chromium generated in the stack and transported by the air stream. In ref. 268, it was shown that the compressive gasket seals in SOFC stacks were colored with Cr deposits, the distribution of which matched the modeling of the Cr evaporation profile from the MICs in contact with the seals according to local O_2 and H_2O partial pressures.

Falk-Windisch et al.²⁶⁹ have reported that oxidation and Cr vaporization have similar rates in the 650–850°C range, but different activation energy values. Thus, although Cr evaporation decreases with lower temperatures, its relative importance with respect to oxidation grows, leading to an observed transition from parabolic to parabolic oxidation at prolonged exposure times. This means that the Cr evaporation process assumes an increasing role for lifetime predictions of steel interconnects as the temperature decreases. An important consequence of these findings is that increasing temperature as a strategy for accelerated degradation analysis and testing of steel interconnects may be somewhat misleading since chemical composition and scale microstructure will significantly change as a function of temperature and also of exposure times.

To prevent Cr evaporation, protective coatings with low electric resistivity and high chemical stability should be used to inhibit its evaporation. Their function is to hinder both oxidation and chromium migration from the substrate steels. The difficulty in the modeling approaches arises from the wide range of testing conditions and the influence of the gas atmosphere. Usually, ex situ characterization methods of protective coatings involve chromium evaporation measurements, ASR measurements, and long-term exposure tests.^{270,271}

Mixed Mn-Co spinels characterized by high conductivity values and good thermal expansion compatibility with ferritic stainless steels are used as protective coating materials.²⁷² To improve lifetime and performance, spinel modification by doping has recently attracted major research attention. Thus, by way of example, in ref. 273, the effect of Fe, Cu, and simultaneous Fe+Cu doping of Mn-Co spinels are studied. A multiple doping approach is proposed as an effective strategy to design cobaltite materials properly tailored for the application.

Despite their importance for a reliable design of accelerated test methods, the development of predictive models for interconnect lifetime has been the subject of a very limited number of works. Simple physical models based on interfacial energy fracture and Cr depletion analysis have been developed by Liu et al.²⁶⁰ and Fang et al.²⁷⁴

to predict the lifetime of coated and uncoated 0.5 mm Crofer 22APU steel. Following the concept that delamination is often observed within the coating layer as a result of CTE mismatch-induced tensile thermal stresses, in ref. 260, service life was predicted by combining oxide growth kinetic data with experimental adhesion/spallation behavior of the oxide scales, which allowed to determine a critical oxide thickness for spallation. The model predicted that uncoated Crofer 22 APU will fail at a chromia scale of 11.2 μm , corresponding to 4750 h of operation at 800°C. A $\text{Mn}_{1.5}\text{Co}_{1.5}\text{O}_4$ spinel-coated Crofer showed a predicted lifetime of 15,500 h with a critical oxide thickness of 4.2 μm , under the same operating conditions.

Feng et al.²⁷⁴ considered a different physical predictive model based on a Cr depletion analysis, which combined diffusion, oxidation, and Cr evaporation experimental data, while the effect of mechanical scale integrity was not taken into consideration. The critical oxide thickness was defined as when Cr concentration at steel/oxide interfaces drops in the critical range of 14–16 wt.%, which causes a transition from protective to a breakaway destructive oxidation. With this model, the estimated lifetime of a $\text{MnCo}_{1.9}\text{Fe}_{0.1}\text{O}_4$ spinel-coated Crofer was more than 35,000 h at 850°C, which is roughly double the lifetime of uncoated Crofer.

Xu et al.²⁷⁵ and Akanda et al.²⁷⁶ have extended the coating mechanical degradation approach proposed by Liu et al.²⁶⁰ by developing an integrated experimental and modeling methodology to predict critical chromia oxide thickness and the consequent lifetime of coated MIC components. Thus, the lifetime of a manganese-cobalt spinel oxide coated 18Cr (441) ferritic stainless steel was estimated by Akanda et al.²⁷⁶ taking into consideration the fracture energy at the interface between the chromia scale and the coating rather than the interfacial shear strength as proposed by Liu et al.²⁶⁰ Comparing interfacial fracture energy from experiments and from an analytical model, the critical chromia thickness at which spinel coating spallation occurs was correlated to the chromia scale growth rate. Despite different calculation methods, lifetime prediction results were very similar to those reported in ref. 260. Thus, 4.2 μm was confirmed as a critical chromia thickness value for spinel coating spallation and as a result, a comparable estimate of spinel coating lifetime of 34,720 h, at 750°C, was determined.

A more refined energy-based fracture analysis is reported in the work of Xu et al.,²⁷⁵ where the critical chromia thickness was determined for a manganese-cobalt spinel coated 441 steel at 800°C as a function of various design factors including the spinel coating thickness. It was found that the critical chromia thickness significantly increases from 4.2 μm (without spinel coating) to about 10 μm (with a 15- μm thick coating). In the latter case, the

projected coated MIC lifetime is extended to about 40,000 h, at 800°C.

A more sophisticated model based on a first-principle approach was described in the work by Oum et al.¹⁷⁹ In this work, a theoretical Cr depletion analysis based on a modified version of the Deal-Grove model²⁷⁷ was developed to predict the lifetime of an uncoated 26 Cr ferritic steel alloy at 850°C. The different fluxes of chromium, water, and chromia are incorporated in the theoretical model to account for the Cr depletion. The model was partly validated with experimental data and predicts that the oxide scale is completely volatilized soon after 3250 h of exposure in air+3H₂O, thus marking the end of the steel useful life. The model also predicts that the lifetime is greatly affected by the humidity content in the air. For instance, the predicted lifetime drastically reduces by nearly half when the humidity rises from 3% to 5%. Thus, the confirmation that humidity is a highly threatening factor for MIC lifetime could make the theoretical model proposed by Oum et al.¹⁷⁹ a valuable tool to be employed for designing well-targeted accelerated degradation tests. Moreover, it is also interesting to observe that, although interconnect oxidation is a very complex degradation process to model theoretically, the results of this model report a useful lifetime of uncoated steels, which is in excellent accordance with the above-mentioned physical prediction models,²⁶⁰ showing in both cases that the useful lifetime of uncoated steels collapses rapidly in less than 5000 h when exposed to temperatures of 800°C or higher.

3 | STACK-LEVEL DEGRADATION

The total degradation of the cell/stack operating at constant conditions can be presented as the sum of the contributions coming from the main components (i.e., electrodes, electrolyte, interconnect, and their interfaces). An SOC can be examined also from different points of view: as a power generator, based on electrochemical reactions at continuum level; as a heat and mass exchanger, in a perspective of fluid dynamics and transport phenomena; as a chemical reactor, in terms of chemical reactions depending on fuel composition and heat effects associated with the electrochemical conversion.²⁷⁸ Modeling an SOC stack, therefore, should focus on several aspects, such as mass transport, heat exchange, charge conduction, reaction mechanisms, and so on, while driving the model results toward the desired function of the stack/system. Due to the complexity of the studied phenomena and components, experimental tests and models on specific separated cell elements are performed to obtain a better understanding of occurring local mechanisms. Still, in these cases, the influence of the other components vanishes and

it is not possible to have an effective overview of the stack process.

In the previous sections, different degradation phenomena, mechanisms, and modeling approaches (mainly at the microscale level) have been presented. However, in complete cell/stack operation there can be overlapping of contributions from different processes. In some cases, combined phenomena can, on the one hand, amplify and accelerate degradation or, on the other hand, lessen their effects. Thus it is useful to investigate in depth the degradation behavior of a specific component/part in the cell/stack (through both experimental procedures and modeling), but the whole system should also be considered to detect the total degradation due to the resultant of different phenomena.^{41,44}

The final goal is to find the relation between degradation and operating conditions, predicting the resulting failures.^{39,279,280} This general approach can ensure degradation prediction based on architecture and system state, for which analyses on cell/stack level at different operating conditions are important. Moreover, since the results of a computational model are only an approximation of real-world conditions and considering that numerical convergence alone is not sufficient, it is worth remarking that experimental validation is a necessary step for both model building, tuning, and validation.^{281–283} In this respect, Wuillemin et al.^{35,36} have highlighted the importance of the use of segmented stack repeating units to assess the local character of performance and degradation as well as the use of such spatially resolved experimental data for the calibration of electrochemical model.⁴⁰

3.1 | Multi-physics numerical simulation (high-level models)

In the available literature, different high-level models are proposed for the complete description of SOC behavior, based on both rigorous theoretical formulations and semi-empirical approaches, where some parameters can be evaluated only through comparison with experimental data.⁴⁰ Due to the complexity of system resolution, different scales of detail are present.

The use of simplified models (e.g., 0D, where the studied system can be described as a single lumped point), allows to have a preliminary overview of occurring mechanisms with a minimum of computational effort,^{284,285} but local phenomena are not evaluated. Therefore, a better understanding can be obtained using higher-dimension models.

In ref. 286, a 2D isothermal model for a planar SOFC is developed to estimate profiles of the main properties in cell cross-section, whereas in a 2D simulation for a tubular SOFC is modeled, solving material, momentum,

charge, and energy balances in cylindrical geometry. A 2D approach for planar SOC is also developed for fuel cells, electrolysis, and pressurized co-electrolysis in refs. 138, 287, and 288. In these cases, the local exchange current densities are computed along the cell length through microscale electrode models taking into account the reaction pathways in both active layers, as described in refs. 18, 183, and 207. This thermo-electrochemical model coupled to mechanical computations¹³⁵ can be used to investigate degradation and the impact on performances.^{18,54,289} As regards SOEC operation, a 2D dynamic model is presented in ref. 290 to estimate tubular SOEC behavior: different electric load variations are considered to estimate cell response time in terms of obtained voltage and temperature.

In refs. 291 and 292, a 3D model for the simulation of planar FC stack performance is introduced, previously validated for molten carbonate fuel cell (MCFC) technologies and then extended to SOFC applications. The model is based on physical principles and its core consists of a semi-empirical electro-kinetic relationship, which has to be tuned through experimental parameter identification processes. Each cell plane is divided into an optimized number of sub-elements, where local mass, energy, charge, and momentum balances are applied, and thermodynamic-kinetic properties are calculated. The main chemical-physical variables characterizing the FC operation are evaluated at the local level for different cells of the stack.

In refs. 280 and 293, a complete SOFC stack modeling framework was presented that combines a thermo-electrochemical model, including degradation processes, with a finite-element thermo-mechanical model that considers rate-independent plasticity and creep of the component materials and shrinkage of the nickel-based negative electrode during thermal cycling. Stresses in both the anode and the cathode contribute to the probability of failure, which can be lowered by adjusting the operating conditions. Gas diffusion layer (GDL) and MIC have a lower impact on the failure probability but affect the contact pressure on the GDLs, which can cause electrical contact loss. Importantly, the requirements for increased mechanical reliability were opposite to those that reduce electrochemical degradation, implying compromises have to be made. Electrochemical degradation modifies the temperature profile under constant system power output and consequently the risks of cell failure. Irreversible deformation of the stack components causes losses of contact pressure during thermal cycling and variation of the electrical load, and increases the risks of anode and cathode cracking. Critical tensile stress develops in the GDC barrier layer (between YSZ and LSCF) during thermal cycling depending on the temperature profile in operation. Counter-flow together with low methane pre-reforming, higher SRU

outlet temperature, and lower system specific power were the most favorable conditions with respect to electrochemical degradation, because this lowers and flattens the oxygen electrode overpotential and minimizes the air blower consumption. These conditions however are unfavorable for mechanical reliability. Conversely, higher pre-reforming rate, higher system specific power, and lower outlet temperature lead to the lowest fuel electrode failure probability. This clearly shows that for the long-term electrical efficiency of a SOFC stack, electrochemical performance must be balanced with mechanical reliability considerations.

In ref. 294, a physics-based procedure combining experiments and multi-physics numerical simulations is developed for the overall analysis of SOFC operational diagnostics and performance predictions. In this procedure, essential information for the fuel cell is extracted first by utilizing empirical polarization analysis and then refined by multi-physics numerical simulations via simultaneous analysis and calibration of polarization curves and impedance behavior. The performance at different utilization cases and operating currents are also predicted to confirm the accuracy of the proposed model. It is demonstrated that, with the present electrochemical model, three air/fuel flow conditions are needed to produce a set of complete data for a better understanding of the processes occurring within SOFCs. After calibration against button cell experiments, the methodology can be used to assess the performance of planar cells without further calibration. The proposed methodology permits to accelerate the calibration process and improves the efficiency of design and diagnostics.

3.2 | System simulation (low-level models) and multiscale modeling

Moving towards full system simulation, that is, stack and auxiliaries (balance of plant components), for different scopes, such as system monitoring, diagnosis, prognosis, and control, model-based and data-driven approaches are generally preferred. For instance, a dynamic lumped modeling approach is applied in ref. 295, where an Integrated Systems Module (ISM) is accounted for. The developed module consists of two SOFC stacks enclosed within a hot-box, through which the stack temperature is kept controlled around a defined set-point. Dynamic lumped energy balances are applied to simulate stack, pre-reformer, afterburner, and heat exchanger temperatures. Such equations account for inlet and outlet energy flows carried by the gases and, in the case of the SOFC stacks, also for the provided electric power. The stack voltage is modeled using the Area Specific Resistance (ASR)

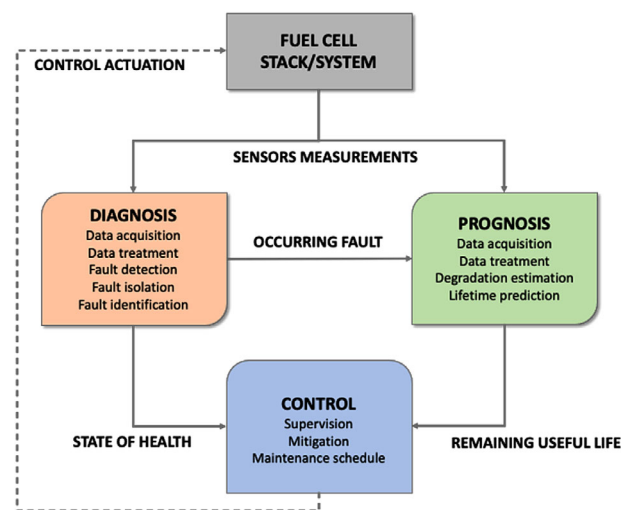


FIGURE 7 Integration among diagnosis, prognosis, and control applied to stacks and systems: different modeling approaches can be applied to each task according to information and measurements availability

approach. A useful contribution in this work is the evaluation of the heat exchanged among the different system components through conduction, convection, and radiation. The parameters required by the model are identified based upon experimental data.

In ref. 296, the 0D dynamic simulation for a SOFC/gas turbine hybrid system considers also SOFC degradation, introducing a coefficient of deterioration increasing with time for the voltage value. In ref. 297, a system simulation approach including degradation was developed in the context of SOFC operation. A lifetime simulation tool was applied to a physical SOFC system model designed and controlled to allow dynamic dispatch. The system was operated in two modes: constant power output and diurnal dynamic dispatch. The dynamically dispatched SOFC system proved more durable and degraded less than a system operated at constant power output.

3.2.1 | Stack state of health: Diagnostics

For operational control, diagnosis tools are developed to avoid premature degradation of the fuel cell (see left branch in Figure 7). The main task of fault diagnosis is to evaluate the deviation of the current state from the normal behavior of the fuel cell (or electrolyser), detecting hazardous states.

The SoH has to be identified by diagnosing these fault modes. To reach this goal, several stages have to be followed: data acquisition, data treatment, and fault detection. In ref. 298, a lumped modeling approach (i.e., no spatial distribution of the main variables within the cells/stack

is described) is used to develop a dynamic SOFC system model applied for diagnostic purposes. Through faulty state simulation, a correlation among faults and operating variables is obtained and summarized in a Fault Signature Matrix, useful for fault detection and isolation purposes. The diagnostic algorithm presented in this work was experimentally validated in ref. 299. An online experimental procedure was applied to a pre-commercial SOFC system where faulty states were induced and validated in controlled conditions.

Data-driven approaches, such as neural networks, as well as multilinear regressions,³⁰⁰ provide the modeling basis on which degradation models and, thus, lifetime prediction tools for performance models can be built.

Statistical and stochastic approaches (e.g., Gaussian Process, Transformed Gamma Process, Non-Homogeneous Gamma Process, Non-Homogeneous Poisson process, Random Walk, and so on) are usually applied to develop advanced remaining useful life (RUL) prediction algorithms. With this aim, stochastic processes can be adapted to model specific degradation behavior, and model parameters can be estimated by suitable inferential procedures applied to measured experimental data. After determining the degradation model, lifetime distribution and prediction procedures for the RUL of a running unit can be provided. Among statistical methods available in the literature, Bayesian methods, Method of Moments, and Maximum Likelihood estimation procedures can be suitably applied to SOC operation. In refs. 301 and 302, Bayesian estimation procedures are used to model degradation processes as Non-Homogeneous Gamma Processes, upon which an RUL probability density function is evaluated. Furthermore, in refs. 303 and 304, Bayesian inferential procedure has been proposed for another useful process, the transformed Wiener process that describes degradation phenomena where degradation increments are not necessarily positive and depend stochastically on the current degradation level. The proposed approach allows to predict the RUL of a unit and can be easily extended to predict SOC lifetime on paper.

Empirical statistical models can also be adopted to cope with variance among units present in the measured SOC data, and to predict degradation and time evolution of parameter values. The approach proposed in ref. 21 provides a basis for accelerated stress tests on SOC technologies.

A correlation between degradation phenomena and fault detection is often introduced to improve control and diagnostic action. In ref. 305, a review is given of SOFC degradation phenomena and corresponding fault detection methodologies. An analysis of the gap in the literature is also performed. In refs. 306 and 307, a hybrid model is introduced (Multiple Model Prognostic Approach) that

combines operational point databases with signal-based methods. It uses a specific structure, where a supervisor manages multiple sub-models related to operating points or intervals and saves operating point/interval-related data from the databases referring to the operating point model. The sub-models have signal-based tools to analyze their data. They investigate the data and the change of operation. The supervisor uses the future current profile and the results of the operating point models to estimate the RUL.

Thus, for the control of SOC stacks and systems, intelligent real-time algorithms can be used that do not require the embedding of high-level models, if the main purpose is safe continuous operation under well-performing conditions. This was demonstrated by a series of studies,^{308–309,310} adopting real-time optimization techniques. Using only fairly basic SOFC stack and system models, accounting for a reformer, a burner, heat exchange, and a heat balance model, they experimentally demonstrated that a commercial SOFC system could be safely controlled within its set of operation limits (maximum current density, minimum cell voltage, maximum stack outlet temperature, maximum fuel utilization, minimum air-fuel ratio, etc.) while keeping it at the optimal performance (in this case at ~65% electrical efficiency) under variable dynamics. The reason for this remarkable achievement is the use of online measurements taken on the system that are included in the feedback control algorithm, allowing to constantly update the underlying models. It is therefore also capable of inherently integrating the degradation processes, since these are part of the online monitoring. This extremely powerful technique is now being extended to SOE operation and proton-exchange membrane (PEM) systems.

3.2.2 | Stack lifetime in real-time: prognostics

In view of a complete cell/stack behavior prediction in real-time applications, also the degradation effects and further performance reduction have to be taken into account. For this purpose, low-level models of specific degradation mechanisms occurring in the main cell elements (referred to in Section 2) are introduced in high-level simulation tools.

For instance, in ref. 41, a 2-D model of planar cell and interconnect is proposed. Mass and energy transport phenomena with electrochemistry are coupled to describe the temperature distribution, changing feeding conditions. Then, in this validated code, also specific equations taking into account possible degradation are added: interconnect corrosion, loss of ionic conductivity, nickel particle growth, Cr contamination, and formation of insulating phases on the oxygen electrode are evaluated.

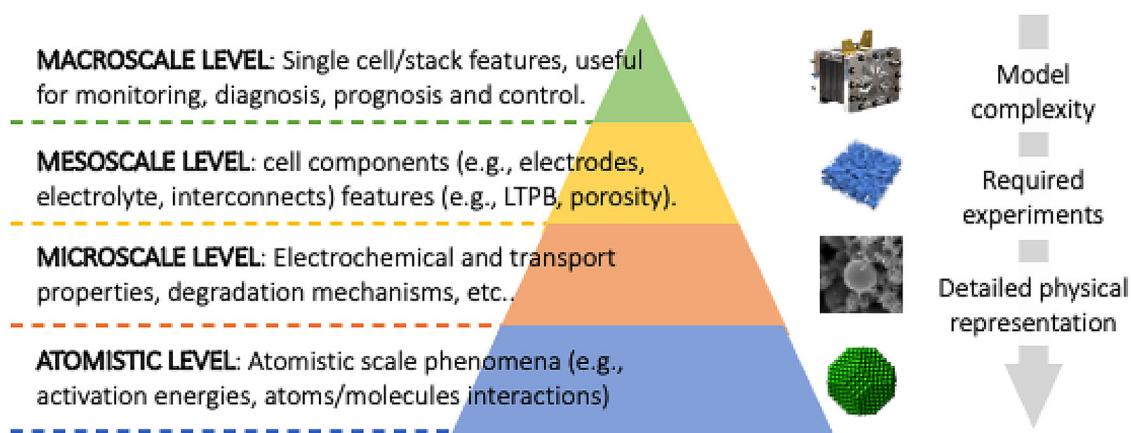


FIGURE 8 The different levels of a fuel cell can be coupled through a multiscale modeling approach; each level (from macroscale to atomistic) requires specific model features as well as experimental data and present an increasing complexity with lower scales

This approach is also followed in ref. 311, where specific equations of cell degradation are paired with a multiphysics model for SOFC electrochemical simulation. The long-term performance is assumed to be influenced by Ni-particle coarsening, oxide scale growth at interconnects, and electrolyte conductivity decrease due to phase transition. Since the degradation phenomena strictly depend on operating conditions, their optimization can reduce cell decay. Hence, in ref. 312, three sub-models are proposed. A process model calculates the system output power as a function of feed and cell features. Considering their dependencies on working conditions, a degradation model simulates the nickel coarsening and oxidation, linked to the deterioration of anodic TPB and conductivity. A third model aims at SOFC optimization: operating conditions are changed so that system lifetime productivity is maximized.

3.2.3 | Integration of high-level and low-level models through multiscale modeling

It is evident from the previous section that, as regards predictive modeling of the complex SOFC system, a multiscale approach is necessary, where microscale and macroscale levels are combined (see Figure 8).

In a critical review of the SoA multiscale models applied in SOFC,²⁷⁸ it is remarked that the challenge for the future is to develop approaches for multiscale multi-physics modeling, considering the coupling of fluid flow, heat transfer, species transport, electrochemical kinetics, and also reforming kinetics (when hydrocarbon fuels are used). For instance, continuum electrochemical models are used to determine the effects of various designs and operating parameters on the generated power, maximum cell temperature, fuel conversion efficiency, stresses caused by

temperature gradients, and thermal expansion. The performance of both the whole system and in particular the electrodes can be calculated, under different operating conditions, since occurring molecular-level mechanisms and material microstructure influences can all be evaluated.

In ref. 313, a multiscale approach is developed, where the microscale electrochemical model (based on Lattice-Boltzmann algorithm) calculates the performance of the porous electrode material, the distribution of reaction surfaces, and the transport of oxygen ions through the material. This detailed electrochemistry modeling is used to evaluate the overall fuel cell current-voltage relation, which becomes the input to the macroscale calculations of the cell current density, voltage, and heat production.

In ref. 314, multiscale modeling is applied to simulate the performance of a SOFC with an axially-graded electrode design. The authors integrate models combining microscale and macroscale features of the whole button cell and its layers. The button cell model is a 1D model addressing electrochemistry and energy balance, with the addition of percolation theory; the cell layers are modeled through a quasi 2D representation of flow fields, fluid dynamics, and thermal dynamics, but with lumped electrochemical phenomena. The integration of the two models is performed through an iterative procedure, computing the voltage with the microscale model and the related current density with the macroscale one, aiming at converging obtained results of the two models.

The work reported in ref. 315 combines microscale representation of electrochemical reactions and transport phenomena with a computational fluid dynamics macroscale model of heat and mass transfer of an SOFC. Experimental data are used to develop the microscale models and to verify the overall performance of the macroscale model.

In ref. 316, an RUL estimation algorithm based on fast modeling of physical degradation of the electrochemical

surface area of a PEMFC is developed. A microscale model is introduced to describe PEMFC catalyst degradation related to Pt agglomeration, simulating Pt particle average size change over time. Then, this information is fed to a macroscale model simulating the overall performance of the PEMFC voltage, where the specific contribution of degradation over cell voltage decay is singled out. Although related to a different technology, this work suitably describes the approach by which a proper RUL estimator for real-time uses can be developed. The model set up in the aforementioned work is then applied in ref. 316 to design a control algorithm for lifetime improvement based on RUL estimation. This approach helps to link the main variables affecting degradation for the definition of suitable control strategies.

4 | CONCLUSIONS AND OUTLOOK

In this review paper, the vast field of research on SOC degradation has been addressed by a systematic approach. First of all, the very definition of degradation and quantification of a degradation rate have been analyzed, highlighting the danger of misinterpretation of reported results and of incomparability of degradation values without a clear indication of the adopted calculation procedure. Various attempts at facilitating a univocal and scientifically robust identification of performance loss over time have been discussed, also taking into account the implications of one-to-one durability testing, with the aim of paving the way for meaningful accelerated stress testing of SOC cells and stacks.

Second, an in-depth and critical assessment of the main degradation processes in three key components of the SOC (negative and positive electrodes and the interconnect) has been carried through, attempting prioritization of respective degradation effects and recommendation of the best approaches in their experimental ascertainment and numerical modeling. The latest advancements in microstructural representation (3D imaging and reconstruction, even touching upon 4D) of SOC electrodes have been reviewed, applied to the quantification of triple-phase boundary (TPB) lengths and morphology evolution over time. Then the key intrinsic degradation processes in the negative (fuel) electrode and the positive (oxygen) electrode have been discussed, covering first the composition and governing mechanisms of the respective electrodes, followed by a comprehensive evaluation of the most important factors of degradation during operation. Particle agglomeration, leading to catalyst depletion, and segregation of species in the functional layer are critical effects at the negative electrode, for which a number of mechanisms have been reviewed. Nickel reoxidation is as

devastating as unpredictable cause for failure in negative electrode-supported SOCs, which has motivated a large number of in-depth studies on the exact processes governing its microstructural effects and possible pathways for mitigation. Overpotential and steam content provide reasons for the enhanced degradation in SOEC mode, also at the positive electrode. The manufacturing stage is particularly important for the latter component, since interdiffusion of chemical elements can take place during sintering of the active and barrier layers. As regards interconnect, excessive oxidation and chromium evaporation are key failure factors in gas-solid interaction, whereas strontium-chromate formation and reactivity with adjacent stack components govern the solid-solid interactions. Of these, the mechanisms of chromium evaporation and reactivity are clearly the most important to harness and control, for which a selection of approaches have been summarized.

Finally, in understanding and capturing the compound microstructural degradation effects on stack and system performance, numerical modeling is a precious tool. Adequate representation of microstructural phenomena needs to trade-off with efficient prognostics of stack behavior and timely intervention when hazardous conditions arise while operating an SOC system. To this effect, high-level multi-physical and low-level lumped models need to merge so that realistic behavior can be predicted reliably and, as much as possible, in real-time. Approaches to this integration can benefit also from practices matured in other technological fields (PEMFC, MCFC, etc.), where multiscale modeling is the only tool to fully capture the complexity of the operating system, subject to the stochastic processes of degradation. In this endeavor, a close interaction between the modeling community and experimental practitioners needs to be constantly promoted.

ACKNOWLEDGMENTS

This work was supported by the Fuel Cells and Hydrogen Joint Undertaking under Grant Agreement number 825027, AD ASTRA. This Joint Undertaking receives support from the European Union's Horizon 2020 research and innovation programme and Hydrogen Europe.

DATA AVAILABILITY STATEMENT

Not Applicable

DECLARATION OF INTEREST

Related to the submitted review paper entitled: Addressing Solid Oxide Cell degradation mechanisms – a critical review

CONFLICT OF INTEREST

The authors have declared no conflict of interest.

ORCID

Stephen J. McPhail  <https://orcid.org/0000-0003-3045-0945>

Hirofumi Uchida  <https://orcid.org/0000-0001-6718-5431>

REFERENCES

- W. Nernst, *Z. Elektrochem.* **1899**, *6*, 41–43.
- E. Baur, H. Preis, *Z. Elektrochem Angew Phys Chem* **1937**, *43*, 727–32.
- H. S. Spacil, C. S. Tedmon Jr. *J. Electrochem. Soc.* **1969**, *116*, 1618–1626.
- W. Dönitz, R. Schmidberger, E. Steinheil, R. Streicher, *Int. J. Hydrogen Energy* **1980**, *5*, 55–63.
- V. Venkataraman, M. Pérez-Fortes, L. Wang, Y. S. Hajimolana, C. Boigues-Muñoz, A. Agostini, S. J. McPhail, F. Maréchal, J. Van Herle, P. V. Aravind, *J. Energy Storage* **2019**, *24*, 100782.
- L. Wang, J. Düll, J. Van herle, F. Maréchal. *Int. J. Hydrogen Energy* **2019**, *44*, 9529–9543.
- H. Yokokawa. *ECS Trans.* **2015**, *68*, 1827–1836.
- A. S. Hagen, in: *Fuel Cells: Data, Facts and Figures*, D. Stolten, R. Can Samsun, N. Garland (Editors) (978-3-527-33240-3) WILEY-VCH, NY, **2016**
- I. Sreedhar, B. Agarwal, P. Goyal, A. Agarwal, *J. Sol. State Electrochem.* **2020**, *24*, 1239–1270. <https://doi.org/10.1007/s10008-020-04584-4>
- H. Yokokawa, H. Kishimoto, T. Shimonosono, K. Yamaji, M. Muramatsu, K. Terada, K. Yashiro, T. Kawada. *J. Electrochem. En. Conv. Stor.* **2017**, *14*, 011004-01
- H. Yokokawa, M. Suzuki, M. Yoda, T. Suto, K. Tomida, K. Hiwataishi, M. Shimazu, A. Kawakami, H. Sumi, M. Ohmori, T. Ryu, N. Mori, M. Iha, S. Yatsuzuka, K. Yamaji, H. Kishimoto, K. Develos-Bagarinao, T. Shimonosono, K. Sasaki, S. Taniguchi, T. Kawada, M. Muramatsu, K. Terada, K. Eguchi, T. Matsui, H. Iwai, M. Kishimoto, N. Shikazono, Y. Mugikura, T. Yamamoto, M. Yoshikawa, K. Yasumoto, K. Asano, Y. Matsuzaki, K. Sato, T. Somekawa. *Fuel Cells* **2019**, *19*, 311–339.
- J. Laurencin, M. Hubert, K. Couturier, T. Le Bihan, P. Cloetens, F. Lefebvre-Joud, E. Siebert, *Electrochim. Acta.* **2015b**, *174*, 1299–1316. <https://doi.org/10.1016/j.electacta.2015.06.080>
- S. Jensen, C. Graves, M. Chen, J. Hansen, X. Sun, *J. Electrochem. Soc.* **2016**, *163*, F1596–F1604. <https://doi.org/10.1149/2.1171614jes>
- A. Ploner, A. Hagen, A. Hauch, *Fuel Cells* **2017**, *17*(4) 498–507. [10.1002/face.201600193](https://doi.org/10.1002/face.201600193)
- N. Akkinapragada, B. Chowdhury, *Carbondale*, IL, USA: Institute of Electrical and Electronics Engineers (IEEE), **2007**, 553–60. <https://doi.org/10.1109/NAPS.2006.359626>
- R. S. Gemmen, M. C. Williams, K. Gerdes, *J. Power Sources* **2008**, *184*(1) 251–259. <https://doi.org/10.1016/j.jpowsour.2008.06.047>
- J. Hjelm. *Degradation Testing – Quantification and Interpretation, Second International Workshop on Degradation Issues of Fuel Cells*, Thessaloniki, Greece, **2011**, 21–23.
- J. Laurencin, M. Hubert, D. Ferreira Sanchez, S. Pylypko, M. Morales, A. Morata et al., *Electrochim. Acta* **2017**, *241*, 459–76. <https://doi.org/10.1016/j.electacta.2017.05.011>
- J. Van herle, D. Perednis, K. Nakamura, S. Diethelm, M. Zahid, A. Aslanides, T. Somekawa, Y. Baba, K. Horiuchi, Y. Matsuzaki, M. Yoshimoto, O. Bucheli, *J. Power Sources* **2008**, *182*, 389–399.
- L. G. J. De Haart, J. Mougin, O. Posdziech, J. Kiviaho, N. H. Menzler, *Fuel Cells* **2009**, *9*(6) 794–804. <https://doi.org/10.1002/face.200800146>
- M. Guida, F. Postiglione, G. Pulcini, **2015a**, *140*, 88–98. <https://doi.org/10.1016/j.res.2015.03.036>
- A. Hagen, R. Barfod, P. V. Hendriksen, Y. L. Liu, S. Ramousse. *J. Electrochem. Soc.* **2006**, *153*, A1165–A1171. <https://doi.org/10.1149/1.2193400>
- P. Tanasini, A. Faes, P. Costamagna, M. Cannarozzo, J. Van herle, A. Hessler-Wyser, C. Comminellis, *Fuel Cells* **2009a**, *9*, 740–752
- A. Ploner, A. Hagen, A. Hauch, *J. Power Sources* **2018**, *395*, 379–385.
- S. Diethelm, J. Van herle, D. Montinaro, O. Bucheli. *Fuel Cells*, **2013**, *13*, 631–637
- FCH JU (Fuel Cells and Hydrogen Joint Undertaking), 2018 ANNUAL WORK PLAN and BUDGET, **2018**, 68. http://www.fch.europa.eu/sites/default/files/FCH2JU2018AWPandBudget_final_11012018.pdf
- L. Blum, P. Batfalsky, Q. Fang, L. G. J. De Haart, J. Malzbender, N. Margaritis, N. Menzler, R. Peters, *ECS Trans.* **2015**, *68*, 157–169.
- SOCTESQA Test Modules, **2015**. <http://www.soctesqa.eu/test-modules>
- ENDURANCE Handbook of Test Procedures and Protocols <http://www.durablepower.eu/index.php/handbook#chapter-1-testing-harmonized-protocols>, **2017**.
- Z. Stoynov, D. Vladikova, B. Burdin, J. Laurencin, D. Montinaro, A. Nakajo, P. Piccardo, A. Thorel, M. Hubert, R. Spotorno, A. Chesnaud. *MRS Advances* **2017**, *2*, 1–13. <https://doi.org/10.1557/adv.2017.592>
- Z. Stoynov, D. Vladikova, B. Burdin, J. Laurencin, D. Montinaro, G. Raikova, G. Schiller, P. Szabo, *Appl. Energy* **2018b**, *228*, 1584.
- V. Haanappel, M. Smith, *J. Power Sources* **2007**, *171*, 169–178
- IEC (International Electrotechnical Commission). Technical Specification 62282-7-2 Single cell/stack performance test methods for solid oxide fuel cells (SOFC), **2013**.
- IEC (International Electrotechnical Commission) International Standard 62282-8-101 Energy storage systems using fuel cell modules in reverse mode – Test procedures for the performance of solid oxide single cells and stacks, including reversible operation, **2020**.
- Z. Wullemin, A. Nakajo, A. Müller, A. J. Schüler, S. Diethelm, J. Van herle, D. Favrat. *ECS Trans.* **2009**, *25*, 457–466, 11th International Symposium on SOFC (SOFC-XI)- 216th ECS Meeting, Vienna, 2009, 4–9.
- Z. Wullemin, Y. Antonetti, C. Beetschen, O. Millioud, S. Ceschini, H. Madi, J. Van herle, *ECS Transactions*, **2013**, *57*, 561–570.
- G. Rinaldi, S. Diethelm, E. Oveisi, P. Burdet, J. Van herle, D. Montinaro, Q. Fu, A. Brisse. *Fuel Cells* **2017**, *17*, 541–549.
- H. Yokokawa, Y. Hori, T. Shigehisa, M. Suzuki, S. Inoue, T. Suto, K. Tomida, M. Shimazu, A. Kawakami, H. Sumi, M. Ohmori, N. Mori, T. Iha, K. Yamaji, H. Kishimoto, K. Develos-Bagarinao, K. Sasaki, S. Taniguchi, T. Kawada, M. Muramatsu, K. Terada, K. Eguchi, T. Matsui, H. Iwai, M. Kishimoto, N. Shikazono, Y. Mugikura, T. Yamamoto, M. Yoshikawa, K. Yasumoto, K. Asano, Y. Matsuzaki, S. Amaha, T.

- Somekawa, *Fuel Cells* **2015**, *15*, 473-497. <https://doi.org/10.1002/fuce.201600186>
39. A. Nakajo, F. Mueller, J. Brouwer, J. Van herle, D. Favrat, *J. Power Sources* **2012a**, *216*, 449-463.
40. A. Nakajo, Z. Wuillemin, P. Metzger, S. Diethelm, G. Schiller, J. Van herle, D. Favrat, *J. Electrochem. Soc.* **2011a**, *158*, B1083-B1101.
41. A. Nakajo, Z. Wuillemin, P. Metzger, S. Diethelm, G. Schiller, J. Van herle, D. Favrat, *J. Electrochem. Soc.* **2011b**, *158*, B1102-B1118.
42. J. A. Schuler, Z. Schuler AJ Wuillemin, A. Hessler-Wyser, C. Ludwig, J. Van herle, *ECS Trans.* **2011a**, *35*, 2001-20081.
43. H. Yokokawa, T. Horita, K. Yamaji, H. Kishimoto, T. Yamamoto, M. Yoshikawa, Y. Mugikura, K. Tomida, *Fuel Cells*. **2013**, *13*, 526-535. <https://doi.org/10.1002/fuce.201200164>
44. A. Nakajo, F. Mueller, J. Brouwer, J. Van herle, D. Favrat. *J. Power Sources* **2012b**, *216*, 434-448.
45. S. J. Kim, P. M. Choi, H. Kim, J. W. Son, J. H. Lee, B. K. Kim, H. W. Lee, S. G. Kim, K. J. Yoon, *J. Power Sources* **2017**, *360*, 284-293. <https://doi.org/10.1016/j.jpowsour.2017.06.004>
46. A. Weber, J. Szász, S. Dierickx, C. Endler-Schuck, E. Ivers-Tiffée, *EIS Trans.* **2015**, *8*, 1953-1960. <https://doi.org/10.1149/06801.1953ecs>
47. H. Djamel, A. Hafsia, Z. Bariza, B. M. Hocine, O. Kafia, *Int. J. Hydrogen Energy* **2013**, *38*, 8575-8583. <https://doi.org/10.1016/j.ijhydene.2013.01.004>
48. A. Nakajo, J. Van herle, D. Favrat, A. Nakajo, J. Van herle, D. Favrat, *Fuel Cells* **2011c**, *11*, 537-552.
49. G. J. Nelson, W. M. Harris, J. J. Lombardo, J. R. Izzo, W. K. S. Chiu, P. Tanasini, M. Cantoni, J. Van herle, C. Comminellis, J. C. Andrews, Y. Liu, P. Pianetta, Y. S. Chu. *Electrochem. Commun.* **2011**, *13*, 586-589.
50. F. Usseglio-Viretta, J. Laurencin, G. Delette, J. Villanova, P. Cloetens, D. Leguillon, *J. Power Sources* **2014**, *256*, 394-403. <https://doi.org/10.1016/j.jpowsour.2014.01.094>
51. P. S. Jørgensen, S. L. Ebbenhøj, A. Hauch, *J. Power Sources* **2015**, *279*, 686-693. <https://doi.org/10.1016/j.jpowsour.2015.01.054>
52. A. Nakajo, A. Cocco, M. De Gostin, A. Peracchio, B. Cassenti, M. Cantoni, J. Van Herle, W. K. S. Chiu, *J. Power Sources* **2016**, *325*, 786-800. <https://doi.org/10.1016/j.jpowsour.2016.06.046>
53. M. Hubert, J. Laurencin, P. Cloetens, J. Mouglin, D. Ferreira Sanchez, S. Pylypko, M. Morales, A. Morata, B. Morel, D. Montinaro, E. Siebert, F. Lefebvre-Joud, *ECS Trans.* **2017**, *78*, 3167-3177. <https://doi.org/10.1149/07801.3167ecst>
54. M. Hubert, J. Laurencin, P. Cloetens, *J. Power Sources* **2018**, *397*, 240-251. <https://doi.org/10.1016/j.jpowsour.2018.06.097>
55. H. Moussaoui, J. Laurencin, Y. Gavet, G. Delette, M. Hubert, P. Cloetens, T. Le Bihan, J. Debayle, *Comput. Mater. Sci.*, **2018**, *143*, 262-276. <https://doi.org/10.1016/j.commatsci.2017.11.015>
56. H. Moussaoui, J. Debayle, Y. Gavet, P. Cloetens, J. Laurencin, *Powder Technol.*, **2020**, *367*, 67-81.
57. M. Neumann, J. Staněk, O. M. Pecho, L. Holzer, V. Beneš, V. Schmidt, *Comput. Mater. Sci.*, **2016**, *118*, 353-364. <https://doi.org/10.1016/j.commatsci.2016.03.013>
58. R. Spotorno, T. Ferrari, C. Nicolella, P. Piccardo, Proceedings of the 12th European SOFC & SOE Forum, **2016**, Lucerne/Switzerland, B1216.
59. J. Villanova, J. Laurencin, P. Cloetens, P. Bleuet. *J. Power Sources* **2018**, *382*, 199-199. <https://doi.org/10.1016/j.jpowsour.2018.02.043>
60. T. M. M. Heenan, X. Lu, F. Iacoviello, J. B. Robinson, D. J. L. Brett, P. R. Shearing, *J. Electrochem. Soc.*, **2018**, *165*, F921-F931.
61. P. Costamagna, P. Costa, V. Antonucci, *Electrochim. Acta* **1998**, *43*, 375-394. [https://doi.org/10.1016/S0013-4686\(97\)00063-7](https://doi.org/10.1016/S0013-4686(97)00063-7)
62. M. A. Laguna-Bercero, *J. Power Sources* **2012**, *203*, 4-16. <https://doi.org/10.1016/j.jpowsour.2011.12.019>
63. P. Moçoteguy, A. Brisse, *Int. J. Hydrogen Energy* **2013**, *38*, 15887-15902.
64. M. B. Mogensen, M. Chen, H. L. Frandsen, C. Graves, J. B. Hansen, K. V. Hansen, A. Hauch, T. Jacobsen, S. H. Jensen, T. L. Skafte, X. Sun, *Clean Energy*, **2019**, *3*, 175-201.
65. M. N. Ni, M. K. H. Leung, D. Y. C. Leung, *Int. J. Hydrogen Energy* **2008**, *33*, 2337-2354
66. H. Yokokawa, H. Tu, B. Iwanschitz, A. Mai. *J. Power Sour.* **2008**, *182*, 400-412.
67. A. Faes, A. Hessler-Wyser, A. Zryd, J. Van herle, *Membranes*, **2012**, *2*, 585-664.
68. M. A. Laguna-Bercero, V. M. Orera, *Int. J. Hydrogen Energy* **2011**, *36*, 13051-13058.
69. J. Schefold, A. Brisse, *Int. J. Hydrogen Energy* **2017**, *42*, 13415-13426.
70. M. Kusnezoff, N. Trofimenko, M. Müller, A. Michaelis, *Materials* **2016**, *9*, 906. <https://doi.org/10.3390/ma9110906>
71. H. Uchida, N. Osada, M. Watanabe, *Electrochem. Solid-State Lett.*, **2004**, *7*, A500-A502. <https://doi.org/10.1149/1.1819864>
72. Y. Zheng, J. Wang, B. Yu, W. Zhang, J. Chen, J. Qiao, J. Zhang. *Chem. Soc. Rev.*, **2017**, *46*, 1427-1463.
73. Q. Jeangros, A. Faes, J. B. Wagner, T. W. Hansen, U. Aschauer, J. Van herle, A. Hessler-Wyser, R. E. Dunin-Borkowski. *Acta Mater.* **2010**, *58*, 4578-4589.
74. S. Baek, J. Bae, *Int. J. Hydrogen Energy* **2011**, *36*, 689. <https://doi.org/10.1016/j.ijhydene.2010.08.050>
75. A. Satikaya, V. Petrovsky, F. Dogan, *Int. J. Hydrogen Energy* **2012**, *37*, 11370. <https://doi.org/10.1016/j.ijhydene.2012.05.007>
76. T. Talebi, M. Sarrafi, M. Haji, B. Raissi, A. Maghsoudipour, *Int. J. Hydrogen Energy* **2010**, *35*, 9440. <https://doi.org/10.1016/j.ijhydene.2010.04.156>
77. S. W. Cheng, C. H. Tsai, S. H. Wu, C. K. Liu, Y. N. Cheng, R. Y. Lee, *Int. J. Hydrogen Energy* **2015**, *40*, 1534. <https://doi.org/10.1016/j.ijhydene.2014.11.034>
78. Q. Jeangros. In situ TEM study of reduction and reoxidation of NiO/ceramic composites EPFL PhD thesis, **2014**, 6376.
79. Q. Jeangros, T. W. Hansen, J. B. Wagner, C. D. Damsgaard, R. E. Dunin-Borkowski, C. Hébert, J. Van herle, A. Hessler-Wyser, *J Mat Sci.* **2013**, *48*, 2893-2907.
80. Z. Jiao, N. Shikazono. *J. Electrochem. Soc.* **2015**, *162*, F571-F578. <https://doi.org/10.1149/2.0721506jes>
81. T. Kawasaki, J. Sugimoto, Y. Tachikawa, Y. Shiratori, S. Taniguchi, K. Sasaki, *ECS Trans.* **2015**, *68*, 1345-1352. <https://doi.org/10.1149/06801.1345ecst>
82. M. Khan, S. Lee, R. Song, J. Lee, T. Lim, S. Park, *Ceram. Int.* **2016**, *42*, 35-48. <https://doi.org/10.1016/j.ceramint.2015.09.006>
83. S. L. Ebbelhoja, T. Ramosa, M. Mogensen, *ECS Trans.* **2012**, *45(1)* 363-375. <https://doi.org/10.1149/1.3701328>
84. P. Holtappels, L. G. J. De Haart, U. Stimming, *J. Electrochem. Soc.* **1999**, *146*, 2976 <https://doi.org/10.1149/1.1392038>
85. J. Mizusaki, H. Tagawa, T. Saito, T. Yamamura, K. Kamitani, K. Hirano, S. Ehara, T. Takagi, T. Hikita, M. Ippommatsu, S. Nakagawa, K. Hashimoto, *Solid State Ionics*, **1994**, *70-71*. 52-58. [https://doi.org/10.1016/0167-2738\(94\)90286-0](https://doi.org/10.1016/0167-2738(94)90286-0)

86. B. De Boer. SOFC anode: hydrogen oxidation at porous nickel and nickel/zirconia electrodes (PhD Thesis), University of Twente, Netherlands, **1998**. <http://purl.utwente.nl/publications/9195>
87. M. Vogler, A. Bieberle-Hütter, L. Gauckler, J. Warnatz, W. G. Bessler, *J. Electrochem. Soc.* **2009**, *156*, B663. <https://doi.org/10.1149/1.3095477>
88. W. G. Bessler, M. Vogler, H. Störmer, D. Gerthsen, A. Utz, A. Weber, E. Ivers-Tiffée, *Phys. Chem. Chem. Phys.* **2010**, *12*, 13888. <https://doi.org/10.1039/c0cp00541j>
89. D. G. Goodwin, H. Zhu, A. M. Colclasure, R. J. Kee, *J. Electrochem. Soc.* **2009**, *156*, B1004. <https://doi.org/10.1149/1.3148331>
90. S. I. Bredikhin, D. A. Agarkov, A. S. Aronin, I. N. Burmistrov, D. V. Matveev, V. V. Kharton, *Mater. Lett.* **2018**, *216*, 193–195. <https://doi.org/10.1016/j.matlet.2018.01.022>
91. Z. Fu, M. Wang, P. Zuo, Z. Yang, R. Wu, *Phys. Chem. Chem. Phys.* **2014**, *16*, 8536–8540. <https://doi.org/10.1039/C3CP55076A>
92. M. Mogensen, J. Høgh, K. V. Hansen, T. Jacobsen, *ECS Trans.* **2007**, *7*, 1329–1338. <https://doi.org/10.1149/1.2729236>
93. F. Monaco, M. Hubert, J. Vulliet, J. P. Ouweltjes, D. Montinaro, P. Cloetens, P. Piccardo, F. Lefebvre-Joud, J. Laurencin, *J. Electrochem. Soc.*, **2019**, *166*, F1229–F1242.
94. A. Faes, A. Hessler-Wyser, D. Presvytes, C. G. Vayenas, J. Van herle, *Fuel Cells*, **2009a**, *9*(6), 841–851. <https://doi.org/10.1002/face.200800147>
95. R. Vaßen, D. Simwonis, D. Stöver, *J. Mater. Sci.* **2001**, *36*, 147–151. <https://doi.org/10.1023/A:100484932>
96. M. Ananyev, D. Bronin, D. Osinkin, V. Eremin, R. Steinberger-Wilckens, L. G. J. De Haart, J. Mertens *J. Power Sources*, **2015**, *286*, 414–426. <https://doi.org/10.1016/j.jpowsour.2015.03.168>
97. D. Kennouche, Y. Wiegart, K. Kremski, J. Wang, J. Gibbs, P. Voorhees, S. Barnett, *Acta Mater.* **2016**, *103*, 204–210. <https://doi.org/10.1016/j.actamat.2015.09.055>
98. J. Villanova, S. Schlabach, A. Brisse, A. Léon. *J. Power Sources* **2019**, *421*, 100–108.
99. A. Nakajo, A. Cocco, M. B. Degostin, P. Burdet, A. A. Peracchio, B. N. Cassenti, M. Cantoni, J. Van Herle, W. K. S. Chiu, *ECS Trans.*, **2017**, *78*, 3205–3215
100. K. Thyden, Y. L. Liu, J. B. Bilde-Sørensen, *Solid State Ionics* **1984**, *2008*, 178.
101. A. Hagen, J. F. B. Rasmussen, K. Thyden, *J. Power Sources* **2011**, *196*, 7271.
102. X. Sun, M. Chen, P. Hjalmarsen, Y. Liu, S. Ebbesen, S. Jensen, M. Mogensen, P. Hendriksen, *J. Electrochem. Soc.*, **2013**, *160*, F1074–F1080.
103. M. Rao, X. Sun, A. Hagen. *ECS Transactions*, *232nd ECS Meeting*, National Harbor MD, **2017**, *80*, 57–69.
104. G. Rinaldi, A. Nakajo, P. Burdet, M. Cantoni, W. K. S. Chiu, J. Van herle, *Acta Mater.* **2019a**, *178*, 194–206.
105. A. Hauch, S. D. Ebbesen, S. H. Jensen, M. Mogensen, *J. Electrochem. Soc.* **2008**, *155*, B1184–B1193. <https://doi.org/10.1149/1.2967331>.
106. M. Trini, A. Hauch, S. De Angelis, X. Tong, P. Vang Hendriksen, M. Chen, *J. Power Sources* **2020**, *450*, 227599.
107. L. Holzer, B. Iwanschitz, T. Hocker, B. Münch, M. Prestat, D. Wiedenmann, U. Vogt, P. Holtappels, J. Sfeir, A. Mai, T. Graule, *J. Power Sources* **2011**, *196*, 1279–1294.
108. Z. Jiao, N. Takagi, N. Shikazono, N. Kasagi. *J. Power Sources* **2011**, *196*, 1019–1029.
109. Y. H. Lee, H. Muroyama, T. Matsui, K. Eguchi, *J. Power Sources* **2014**, *262*, 451–456.
110. A. Nakajo, J. Kuebler, A. Faes, U. F. Vogt, H. J. Schindler, L. K. Chiang, S. Modena, J. Van herle, T. Hocker, *Ceram. Int.* **2012c**, *38*, 3907–3927.
111. A. Faes, A. Nakajo, A. Hessler-Wyser, D. Dubois, A. Brisse, S. Modena, J. Van herle, *J. Power Sources* **2009b**, *193*(1), 55–64.
112. A. Faes, Z. Wuillemin, P. Tanasini, N. Accardo, J. Van herle, *J. Power Sources*, **2011b**, *196*, 3553–3558
113. X. Mantzouris, N. Zouvelou, D. Skarmoutsos, P. Nikolopoulos, *J. Mater. Sci.* **2005**, *40*, 2471–2475.
114. M. C. Munoz, S. Gallego, J. I. Beltran, J. Cerda, *Surf. Sci. Rep.* **2006**, *61*, 303–344.
115. A. Tsoga, P. Nikolopoulos, A. Naoumidis. *Ionics* **1996**, *2*, 427–434.
116. H. Y. Chen, H. C. Yu, J. S. Cronin, J. R. Wilson, S. A. Barnett, K. Thornton, *J. Power Sources* **2011**, *196*, 1333–1337.
117. J. Sehested, *Catal. Today* **2006**, *III*, 103–110.
118. S. Gao, J. Li, Z. Lin, *J. Power Sources* **2014**, *255*, 144–150.
119. A. Hauch, M. Mogensen, A. Hagen. *Solid State Ionics* **2011**, *192*(1) 547–551. <https://doi.org/10.1016/j.ssi.2010.01.004>
120. L. Kröll, L. G. J. De Haart, I. Vinke, R. A. Eichel, *Phys. Rev. Applied* **2017**, *7*, 044007.
121. M. Z. Khan, M. T. Mehran, R. H. Song, J. W. Lee, S. B. Lee, T. H. Lim, *J. Power Sources* **2018**, *391*, 94–105.
122. J. Mason, I. Celik, S. Lee, H. Abernathy, G. Hackett, *J. Electrochem. Soc.* **2018**, *165*, F64–F74.
123. D. Simwonis, F. Tietz, D. Stover, *Solid State Ionics* **2000**, *132*, 241–251.
124. F. Abdeljawad, B. Völker, R. Davis, R. M. McMeeking, M. Haataja, *J. Power Sources*, **2014**, *250*, 319–331.
125. M. Trini. Characterization and Modelling of Microstructure Evolution in Ni/Yttria Stabilized Zirconia Hydrogen Electrodes for High Temperature Solid Oxide Cells, Ph.D. Thesis, DTU, **2009**.
126. E. Lay-Grindler, J. Laurencin, J. Villanova, P. Cloetens, P. Bleuet, A. Mansuy, J. Mougín, G. Delette, *J. Power Sources* **2014**, *269*, 927–936.
127. M. Mogensen, A. Hauch, X. Sun, M. Chen, Y. Tao, S. Ebbesen, K. Hansen, P. Hendriksen, *Fuel Cells* **2017**, *17*, 434–441. <https://doi.org/10.1002/face.201600222>
128. A. Nakajo, G. Rinaldi, P. Caliandro, G. Jeanmonod, L. Navratilova, M. Cantoni, J. Van herle. *J. Electrochem Energy Conversion Storage* **2020**, *17*, 041102, doi [10.1115/1.4046478](https://doi.org/10.1115/1.4046478)
129. A. Hauch, K. Brodersen, M. Chen, M. B. Mogensen. *Solid State Ionics*, **2016**, *293*, 27–36.
130. G. Rinaldi, A. Nakajo, P. Caliandro, L. Navratilova, *ECS Trans.* **2019b**, *91*, 641.
131. M. W. Finnis, *J. Phys. Condens. Matter* **1996**, *8*, 5811–5836.
132. A. Nakajo, Z. Wuillemin, J. Van herle, D. J. Favrat. *Power Sources* **2009a**, *193*, 203–215.
133. A. Nakajo, A. M. Kiss, A. P. Cocco, W. M. Harris, M. B. DeGostin, F. Greco, G. J. Nelson, A. A. Peracchio, B. N. Cassenti, A. Deriy, S. Wang, Y. C. K. Chen-Wiegart, J. Wang, J. Van herle, W. K. S. Chiu, *ECS Trans.* **2015**, *68*, 1069–1081.
134. A. Nakajo, J. Van herle, D. Favrat, in: Irvine J, Connor P (eds) *Solid Oxide Fuels Cells: Facts and Figures. Green Energy and Technology*. Springer, London, **2013**, *55*, 121–162 https://doi.org/10.1007/978-1-4471-4456-4_6 ISBN 978-1-4471-4455-7.

135. J. Laurencin, G. Delette, F. Lefebvre-Joud, M. Dupeux, *J. Euro. Ceram. Soc.* **2008a**, *28*, 1857-1869.
136. F. Greco, A. Nakajo, Z. Wuillemin, J. Van herle, *ECS Trans.* **2015**, *68*, 1921-1931.
137. J. Laurencin, G. Delette, F. Usseglio-Viretta, S. Di Iorio, *J. Euro. Ceram. Soc.* **2011a**, *31*, 1741-1752.
138. J. Laurencin, G. Delette, F. Usseglio-Viretta, S. Di Iorio, F. Lefebvre-Joud, *ECS Trans.*, **2011b**, *35*, 1463-1471.
139. F. Greco, H. L. Frandsen, A. Nakajo, M. F. Madsen, J. Van herle, *J. Eur. Ceram. Soc.*, **2014**, *34*, 2695-2704.
140. J. Kirtley, M. McIntyre, D. Halat, R. Walker, *ECS Trans.* **2013**, *50*, 3-15. <https://doi.org/10.1149/05044.0003ecst>
141. N. Tikekar, T. Armstrong, A. Virkar, *J. Electrochem. Soc.* **2006**, *153*, A654-A663. <https://doi.org/10.1149/1.2167949>
142. Q. Jeangros, T. W. Hansen, J. B. Wagner, R. E. Dunin-Borkowski, C. Hébert, J. Van herle, *Ultramicroscopy* **2016**, *169*, 11-21.
143. A. Faes, Q. Jeangros, J. B. Wagner, T. W. Hansen, J. Van herle, A. Brisse, R. Dunin-Borkowski, A. Hessler-Wyser *ECS Trans.*, **2009c**, *25*, 1985-1992, 11th International Symposium on SOFC (SOFC-XI)- 216th ECS Meeting; Vienna; 4-9 Oct 2009.
144. J. Laurencin, V. Roche, C. Jaboutian, I. Kieffer, J. Mougín, M. C. Steil, *Int. J. of Hydrogen Energy*, **2012**, *37*, 12557-12573.
145. J. L. Young, V. I. Birss, *J. Power Sources* **2011**, *196*, 7126-7135.
146. M. Ettler, H. Timmermann, J. Malzbender, A. Weber, N. H. Menzler, *J. Power Sources* **2010**, *195*, 5452-5467.
147. A. Kiss, W. Cocco, M. Harris, F. De Gostin, N. Greco, A. Peracchio, B. Cassenti, A. Deriy, S. Wang, Y. Wiegart, J. Wang, J. Van Herle, W. K. S. Chiu, *ECS Trans.* **2015**, *68*(1) 1069-1081. <https://doi.org/10.1149/06801.1069ecst>
148. J. Laurencin, G. Delette, B. Morel, F. Lefebvre-Joud, M. Dupeux, *J. Power Sources*, **2009**, *192*, 344-352.
149. J. Malzbender, E. Wessel, R. W. Steinbrech, *Solid State Ionics* **2005**, *176*, 2201-3.
150. A. Faes, J. -. M. Fuerbringer, D. Mohamedi, A. Hessler-Wyser, G. Caboche, J. Van herle, *J. Power Sources*, **2011a**, *196*, 7058-7069.
151. A. Faes, Z. Wuillemin, P. Tanasini, N. Accardo, S. Modena, H. J. Schindler, M. Cantoni, H. Lübke, S. Diethelm, A. Hessler-Wyser, J. Van herle, *J. Power Sources* **2011c**, *196*, 8909-8917.
152. J. Laurencin, G. Delette, O. Sicardy, S. Rosini, F. Lefebvre-Joud, *J. Power Sources*, **2010**, *195*, 2747-2753.
153. D. Fouquet, A. C. Müller, A. Weber, E. Ivers-Tiffée, *Ionics* **2003**, *9*, 103-108.
154. J. Young, H. Molero, V. Birss, *J. Power Sources* **2014**, *271*, 538. <https://doi.org/10.1016/j.jpowsour.2014.07.174>.
155. D. Vladikova, Z. Stoyanov, Z. Wuillemin, D. Montinaro, P. Piccardo, I. Genov, M. Rolland, *ECS Trans.* **2015**, *68*, 1161. <https://doi.org/10.1149/06801.1161ecst>
156. J. Kim, H. I. Ji, H. P. Dasari, D. Shin, H. Song, J. H. Lee, B. K. Kim, H. J. Je, H. W. Lee, K. J. Yoon, *Int. J. Hydrogen Energy* **2013**, *38*, 1225-1235, <https://doi.org/10.1016/j.ijhydene.2012.10.113>
157. A. Mai, V. Haanappel, S. Uhlenbruck, F. Tietz, D. Stover, *Solid State Ionics* **2005**, *176*, 1341-1350.
158. B. Kenney, K. Karan, *Solid State Ionics* **2007**, *178*, 297-306. <https://doi.org/10.1016/j.ssi.2006.12.009>
159. C. Lalanne, G. Prospero, J. M. Bassat, F. Mauvy, S. Fourcade, P. Stevens, M. Zahid, J. Van herle, J. C. Grenier, *Power Sources* **2008**, *185*, 1218-1224.
160. A. Tarancon, M. Burriel, J. Santiso, S. J. Skinner, J. A. Kilner, *J. Mater. Chem.* **2010**, *20*, 3799-3813.
161. D. J. L. Brett, A. Atkinson, N. P. Brandon, S. J. Skinner, *Chem. Soc. Rev.* **2008**, *37*, 1568-1578.
162. J. C. Grenier, J. M. Bassat, F. Mauvy, J. A. Kilner, S. J. Skinner, S. J. C. Irvine, P. P. Edwards (Eds.), *Functional Materials for Sustainable Energy Applications*, Woodhead Publishing Series in Energy, **2012**, *35*, 402-444
163. V. Vibhu, A. Rougier, C. Nicollet, A. Flura, J. C. Grenier, J. M. Bassat, *Solid State Ionics* **2015**, *278*, 32-37.
164. J. M. Bassat, M. Burriel, O. Wahyudi, R. Castaing, M. Cerreti, P. Veber, I. Weill, A. Villesuzanne, J. C. Grenier, W. Paulus, J. ., Kilner, *J. Phys. Chem. C.* **2013**, *117*, 26466-26472.
165. S. Saher, J. Song, V. Vibhu, C. Nicollet, A. Flura, J. M. Bassat, H. J. M. Bouwmeester, *J. Mater. Chem. A*, **2018**, *6*, 8331-8339.
166. S. B. Adler, J. A. Lane, B. C. H. Steele, *J. Electrochem. Soc.* **1996**, *143*, 3554. <https://doi.org/10.1149/1.1837252>
167. F. S. Baumann, J. Fleig, H. U. Habermeier, J. Maier, *Solid State Ionics.* **2006**, *177*, 1071-1081. <https://doi.org/10.1016/j.ssi.2006.02.045>
168. S. B. Adler, *Chem. Rev.* **2004**, *104*, 4791-4843. <https://doi.org/10.1021/Cr020724o>
169. J. Laurencin, J. Mougín, In: "Hydrogen Production by Electrolysis", Ed. A. Godula-Jopek, Wiley, NY, **2015a**, 197-208.
170. F. Monaco, V. Tezyk, E. Siebert, S. Pylpko, B. Morel, J. Vulliet, T. Le Bihan, F. Lefebvre-Joud, J. Laurencin, *Solid State Ionics*, **2018**, *319*, 234-246. <https://doi.org/10.1016/j.ssi.2018.02.012>
171. E. Effori, H. Moussaoui, F. Monaco, R. K. Sharma, J. Debayle, Y. Gavet, G. Delette, G. Si Larbi, E. Siebert, J. Vulliet, L. Dessemond, J. Laurencin, *Fuel Cells* **2019**, *19*, 429-444 <https://doi.org/10.1002/fuce.201800185>
172. S. J. Kim, K. J. Kim, G. M. Choi, *Int. J. Hydrogen Energy*, **2015**, *40*, 9032-38.
173. C. E. Frey, Q. Fang, D. Sebold, L. Blum, N. H. Menzler, *J. Electrochem. Soc.* **2018**, *165*, F357-F364.
174. P. Hjalmarsson, M. Sogaard, M. Mogensen, *Solid State Ionics*, **2008**, *179*, 1422-1426.
175. E. Bucher, W. Sitte, *Solid State Ionics*, **2011**, *192*, 480-482
176. D. Oh, D. Gostovic, E. D. Wachsman, *J. Mater. Res.*, **2012**, *27*, 1992-1999.
177. C. Endler, A. Leonide, A. Weber, F. Tietz, E. J. Ivers-Tiffée, *Electrochem. Soc.*, **2010**, *157*, B292-B298.
178. T. Horita, D. Cho, F. Wang, M. Nishi, T. Shimonosono, H. Kishimoto, K. Yamaji, M. E. Brito, H. Yokokawa, *ECS Trans.* **2012**, *42*(1) 297-304. <https://doi.org/10.1149/1.4705506>
179. M. Oum, J. Andrews, R. Steinberger-Wilckens, *ECS Trans.* **2017**, *78*, 1565-1574. <https://doi.org/10.1149/07801.1565ecst>
180. J. A. Schuler, Z. Wuillemin, A. Hessler-Wyser, J. Van herle, *ECS Trans.* **2009**, *25*, 2845-2852, 11th International Symposium on SOFC (SOFC-XI)- 216th ECS Meeting; Vienna; 4-9 2009.
181. J. A. Schuler, Z. Wuillemin, A. Hessler-Wyser, J. Van herle, *Electrochem. Solid-State Lett.*, **2011b**, *14*, B20-B22.
182. J. A. Schuler, H. Yokokawa, C. F. Calderone, Q. Jeangros, Z. Wuillemin, A. Hessler-Wyser, J. Van herle, *J. Power Sources* **2012b**, *210*, 112-120.
183. E. Lay-Grindler, J. Laurencin, J. Villanova, I. Kieffer, F. Usseglio-Viretta, T. Le Bihan, P. Bleuët, A. Mansuy, G. Delette, *ECS Trans.* **2013a**, *57*, 3177-3187.

184. T. Shimura, A. He, N. Shikazono, *J. Electrochem. Soc.*, **2019**, *166*, F821-F830.
185. H. Wang, K. J. Yakal-Kremiski, T. Yeh, G. M. Rupp, A. Limbeck, J. Fleig, S. A. Barnett, *J. Electrochem. Soc.*, **2016**, *163*, F581-F585.
186. S. P. Simner, M. D. Anderson, M. H. Engelhard, J. W. Stevenson, *Electrochem. Solid-State Lett.* **2006**, *9*, A478-A481.
187. J. S. Hardy, J. W. Templeton, D. J. Edwards, Z. Lu, J. W. Stevenson, *J. Power Sources* **2012**, *198*, 76-82.
188. C. Nicollet, J. Waxin, T. Dupeyron, A. Flura, J. M. Heintz, J. P. Ouweltjes, P. Piccardo, A. Rougier, J. C. Grenier, J. M. Bassat, *J. Power Sources*, **2017**, *372*, 157-165. <https://doi.org/10.1016/j.jpowsour.2017.10.064>
189. S. Wang, T. Kato, S. Nagata, T. Honda, T. Kaneko, N. Iwashita, M. Dokiya, *Solid State Ionics*, **2002**, *146*, 203-210. [https://doi.org/10.1016/S0167-2738\(01\)01015-3](https://doi.org/10.1016/S0167-2738(01)01015-3)
190. W. Chen, T. Wen, H. Nie, R. Zheng, *Mater. Res. Bull.*, **2003**, *38*, 1319-1328. [https://doi.org/10.1016/S0025-5408\(03\)00143-0](https://doi.org/10.1016/S0025-5408(03)00143-0)
191. S. I. Lee, M. Park, J. Hong, H. Kim, J. W. Son, J. H. Lee, B. K. Kim, H. W. Lee, K. J. Yoon, *J. Eur. Ceram. Soc.*, **2017**, *37*, 3219-3223. <https://doi.org/10.1016/j.jeurceramsoc.2017.03.041>
192. S. Lee, S. Lee, H. J. Kim, S. M. Choi, H. An, M. Y. Park, J. Shin, J. H. Park, J. Ahn, D. Kim, Ji Hi, H. Kim, J. S. Son, J. H. Lee, B. K. Kim, H. W. Lee, J. Hong, D. Shin, K. J. Yoon, *J. Mater. Chem. A*, **2018**, *6*, 15083-15094. <https://doi.org/10.1039/c8ta04974brsc.li/materials-a>
193. F. Tietz, Q. X. Fu, V. A. C. Haanappel, A. Mai, N. H. Menzler, S. Uhlenbruck, *Inter. J. Appl. Ceram. Technol.*, **2007**, *4*(5) 436-445.
194. S. Uhlenbruck, T. Moskalewicz, N. Jordan, H. J. Penkalla, H. P. Buchkremer, *Solid State Ionics*. **2009**, *180*, 418-423.
195. F. Wang, M. E. Brito, K. Yamaji, D. H. Cho, M. Nishi, H. Kishimoto, T. Horita, H. Yokokawa. *Solid State Ionics* **2014**, *262*, 454-459.
196. T. Matsui, S. Li, Y. Inoue, N. Yoshida, H. Muroyama, K. Eguchi, *J. Electrochem. Soc.*, **2019**, *166*, F295-F300.
197. D. Ferreira-Sanchez, D. Grolimund, M. Hubert, P. Bleuuet, J. Laurencin, *Int. J. Hydrogen Energy*, **2017**, *42*, 1203-1211.
198. V. Wilde, H. Störmer, J. Szász, F. Wankmüller, E. Ivers-Tiffée, D. Gerthsen, *Appl. Energy Mater.*, **2018**, *1*, 6790-6800.
199. V. Miguel-Pérez, J. P. Ouweltjes, A. Tarancón, D. Montinaro, A. Morata, *ECS Trans.* **2015**, *68*, 1803-1813. <https://doi.org/10.1149/06801.1803ecst>
200. A. Flura, C. Nicollet, V. Vibhu, B. Zeimetz, A. Rougier, J. M. Bassat, J. C. Grenier, *J. Electrochem. Soc.* **2016**, *163*, F523.
201. K. Shimura, H. Nishino, K. Kakinuma, M. E. Brito, H. Uchida. *Electrochim Acta* **2017a**, *225*, 114-120
202. K. Shimura, H. Nishino, K. Kakinuma, M. E. Brito, H. Uchida, *J. Ceram. Soc. Jpn.*, **2017**, *125*, 218-222.
203. M. Kubicek, A. Limbeck, T. Frömling, H. Hutter, J. Fleig, *J. Electrochem. Soc.*, **2011**, *158*, B727-B734.
204. L. Q. Pan, Z. Zhang, X. Zhang, S. H. Chan, *J. Electrochem. Soc.*, **2015**, *162*, F1316-F1323
205. F. Tietz, D. Sebold, A. Brisse, J. Schefold, *J. Power Sour.* **2013**, *223*, 129-135.
206. A. Mahmoud, M. Al Daroukh, M. Lipinska-Chwalek, M. Luysberg, F. Tietz, R. P. Hermann, *Solid State Ionics* **2017**, *312*, 38-43.
207. M. Hubert, J. Laurencin, P. Cloetens, J. C. Da Silva, F. Lefebvre-Joud, P. Bleuuet, A. Nakajo, E. Siebert, *Solid State Ionics* **2016a**, *294*, 90-107.
208. F. Giannici, G. Canu, A. Chiara, M. Gambino, C. Aliotta, A. Longo, V. Buscaglia, A. Martorana, *ACS Appl. Mater. Interfaces* **2017**, *9*, 44466-44477.
209. D. F. Sanchez, D. Grolimund, M. Hubert, P. Bleuuet, J. Laurencin. *Int. J. Hydrogen Energy* **2017**, *42*, 1203-1211.
210. F. Tietz, A. Mai, D. Stöver, *Solid State Ionics*, **2008**, *179*, 1509-1515.
211. D. Kim, J. W. Park, B. H. Yun, J. H. Park, K. T. Lee. *ACS Appl. Mater. Interfaces* **2019**, *11*, 31786-31792.
212. H. Wang, S. A. Barnett, *J. Electrochem. Soc.*, **2018**, *165*, F564-F570.
213. B. Fan, J. Yan, X. Yan. *Solid State Sci.* **2011**, *13*, 1835-9.
214. N. I. Khamidy, J. Laurencin, E. Djurado, *J. Electroanal. Chem.*, **2019**, *849*, 113373.
215. R. K. Sharma, S. K. Cheah, M. Burriel, L. Dessemond, J. M. Bassat, E. Djurado, *J. Mater. Chem. A* **2017**, *5*, 1120-1132.
216. V. Vibhu, A. Flura, A. Rougier, C. Nicollet, J. C. Grenier, J. M. Bassat, *J. Energy Chem* **2020**, *46*, 62-70.
217. C. Nicollet, A. Flura, V. Vibhu, S. Fourcade, A. Rougier, J. M. Bassat, J. C. Grenier, *Int. J. Hydrog. Energ.* **2016**, *41*, 15538-15544
218. R. K. Sharma, N. I. Khamidy, L. Rapenne, F. Charlot, H. Mousaoui, J. Laurencin, E. Djurado, *J. Power Sources*, **2019**, *419*, 171-180.
219. N. I. Khamidy, J. Laurencin, D. Ferreira-Sanchez, F. Monaco, F. Charlot, E. Djurado, *J. Power Sources* **2020**, *450*, 227724.
220. A. J. Schuler, H. Lübke, A. Hessler-Wyser, J. Van herle, *J. Power Sources* **2012c**, *213*, 223-228.
221. W. M. Harris, J. J. Lombardo, M. B. DeGostin, G. J. Nelson, H. Luebbe, A. J. Schuler, J. Van herle, J. C. Andrews, Y. Liu, P. Pianetta, Y. C. K. Chen, J. Wang, W. K. S. Chiu, *Solid State Ionics* **2013**, *237*, 16-21.
222. C. Pellegrielli, Y. L. Huang, J. A. Taillon, L. G. Salamanca-Riba, E. D. Wachsman, *ECS Trans.* **2015**, *68*, 773-784. <https://doi.org/10.1149/06801.0773ecst>
223. M. Yoshikawa, T. Yamamoto, K. Asano, K. Yasumoto, Y. Mugikura. *ECS Trans.* **2015**, *68*, 2199-2208. <https://doi.org/10.1149/06801.2199ecst>
224. F. Wang, K. Yamaji, D. H. Cho, T. Shimonosono, M. Nishi, H. Kishimoto, M. E. Brito, T. Horita, H. Yokokawa, *Fuel Cells*, **2013**, *13*, 520-525.
225. M. Yoshikawa, T. Yamamoto, K. Yasumoto, Y. Mugikura. *ECS Trans.* **2017**, *75*, 13-31.
226. C. C. Wang, S. He, K. Chen, M. R. Rowles, S. Darvish, Y. Zhong, S. P. Jiang. *J. Electrochem. Soc.* **2017**, *164*, F514-F524.
227. T. Horita, D. H. Cho, F. Wang, M. Nishi, T. Shimonosono, H. Kishimoto, K. Yamaji, M. E. Brito, H. Yokokawa. *ECS Trans.* **2013**, *51*(1) 69-77.
228. E. Bucher, C. Gspan, W. Sitte, *Solid State Ionics*, **2015**, *272*, 112-120.
229. T. Daio, P. Mitra, S. M. Lyth, K. Sasaki, *Int. J. Hydrogen Energy*, **2016**, *41*, 12214-12221.
230. X. Sun, M. Chen, P. Hjalmarsson, S. D. Ebbesen, S. H. Jensen, M. Mogensen, P. V. Hendriksen, *ECS Trans.* **2012**, *41*, 77-85. <https://doi.org/10.1149/1.3702414>
231. A. Hagen, K. Neufeld, Y. L. Liu, *J. Electrochem. Soc.* **2010**, *157*, B1343-B1348. <https://doi.org/10.1149/1.3459904>
232. M. Bianco, M. Linder, Y. Larring, F. Greco, J. Van herle. *Fuel Cells*, **2017**, 121-144.

233. W. Z. Zhu, S. C. Deevi. *Mater Sci Eng A* **2003**, 348:227e43. [https://doi.org/10.1016/S0921-5093\(02\)00736-0](https://doi.org/10.1016/S0921-5093(02)00736-0)
234. J. W. Fergus. *Mater Sci Eng A*, **2005**, 397, 271e83. <https://doi.org/10.1016/j.msea.2005.02.047.M>
235. F. Greco, A. Nakajo, Z. Wuillemin, J. Van Herle, *ECS Trans.*, **2017**, 78, 2271-2283.
236. K. Winciewicz, J. Cooper. *J. Power Sources*, **2005**, 140(2), 280–296. <https://doi.org/10.1016/j.jpowsour.2004.08.032>
237. J. Wu, X. Liu. *J. Mater. Sci. Technol.*, **2010**, 26, 293–305. [https://doi.org/10.1016/S1005-0302\(10\)60049-7](https://doi.org/10.1016/S1005-0302(10)60049-7)
238. Z. Yang, K. S. Weil, D. M. Paxton, J. W. Stevenson. *J Electrochem Soc*, **2003**, 150, A1188. <http://doi.org/10.1149/1.1595659>
239. C. Wagner, *J. Electrochem Soc* **1952**, 99, 369-380.
240. B. Hua, J. Pu, W. Gong, J. Zhang, F. Lu, L. Jian, *J. Power Sources* **2008**, 185, 419–422.
241. V. Miguel-Pérez, A. Martínez-Amesti, M. L. Nó, A. Larrañaga, M. I. Arriortua, *Corros. Sci.* **2012**, 60, 38-49.
242. M. Park, J. S. Shin, S. Lee, H. J. Kim, H. An, H. I. Ji, H. Kim, J. W. Son, J. H. Lee, B. K. Kim, H. W. Lee, K. J. Yoon. *Corros. Sci.* **2018**, 134, 17–22. <https://doi.org/10.1016/j.corsci.2018.01.022>
243. A. Nakajo, Z. Wuillemin, J. Van herle, D. J. Favrat, *J. Power Sources* **2009b**, 193, 216-226.
244. M. Bianco, J. P. Ouweltjes, J. Van herle, *Int. J. Hydrogen Energy*, **2019a**, 44(59) 31406-31422.
245. J. C. W. Mah, A. Muchtar, M. R. Somalu, M. J. Ghazali, *Int. J. Hydrogen Energy*, **2017**, 42, 9219–9229. <https://doi.org/10.1016/j.ijhydene.2016.03.195>
246. P. Piccardo, S. Anelli, V. Bongiorno, R. Spotorno, L. Repetto, P. Girardon, *Int. J. Hydrogen Energy* **2015a**, 40, 3726-3738, <https://doi.org/10.1016/j.ijhydene.2015.01.083>
247. V. Bongiorno, P. Piccardo, S. Anelli et al., *Acta Metall. Sin.* **2017**, 30, 697–711. <https://doi.org/10.1007/s40195-017-0543-1>.
248. M. Bianco, J. Tallgren, J. E. Hong, S. Yang, O. Himanen, J. Mikkola, J. Van herle, R. Steinberger-Wilckens, *J. Power Sources*, **2019b**, 437, 226900.
249. G. Jalilvand, M. A. Faghihi-Sani. *Int. J. Hydrogen Energy* **2013**, 38, 12007-12014.
250. R. Spotorno, P. Piccardo, F. Perrozzi, S. Valente, M. Viviani, A. Ansar. *Fuel Cells*, **2015**, 15, 728–734. <https://doi.org/10.1002/fuce.201400189>
251. X. Chen, P. Y. Hou, C. P. Jacobson, S. J. Visco, L. C. De Jonghe. *Solid State Ionics* **2005**, 176, 425–433.
252. M. Bianco, P. Caliandro, S. Diethelm, S. Yang, A. Dellai, J. Van herle, R. Steinberger-Wilckens, *J. Power Sources*, **2020a**, 461, 228163.
253. M. Bianco, S. Poitel, J. E. Hong, S. Yang, Z. J. Wang, M. Willinger, R. Steinberger-Wilckens, *Corros. Sci.*, **2020b**, 108414.
254. D. M. Bastidas, *Rev Metal* **2006**, 42, 425-443; <https://doi.org/10.3989/revmetalm.2006.v42.i6.41>
255. L. Niewolak, F. Tietz, W. J. Quadackers, Interconnects, in K. Kendall, M. Kendall (Eds.) *High-Temperature Solid Oxide Fuel Cells for the 21st Century*, Second Edition, Academic Press, London, UK, **2016**, 195-254. <https://doi.org/10.1016/B978-0-12-410453-2.00007-5>
256. Z. Yang. *Int. Mater. Rev.*, **2008**, 53, 39-53. <https://doi.org/10.1179/174328007X212526>
257. D. Larrain, J. Van herle, D. Favrat, *J. Power Sources* **2006**, 161, 392-403.
258. P. Huczowski, N. Christiansen, V. Shemet, J. Piron-Abellan, L. Singheiser, W. J. Quadackers, *Mater. Corros.*, **2004**, 55(11), 825-830. <https://doi.org/10.1002/maco.200303798>
259. R. Duan, A. Jalowicka, K. Unocic, B. A. Pint, P. Huczowski, A. Chyrkin, D. Grüner, R. Pillai, W. J. Quadackers, *Oxid. Met.* **2017**, 87, 11-38. <https://doi.org/10.1007/s11085-016-9653-9>
260. W. N. Liu, X. Sun, E. Stephens, M. A. Khaleel, *J. Power Sources*, **2009**, 189, 1044-1050. <https://doi.org/10.1016/j.jpowsour.2008.12.143>
261. A. Hessler-Wyser et al, *J. Mater. Sci.*, **2011**, 46, 4532–4539. <https://doi.org/10.1007/s10853-011-5347-5>.
262. S. P. Jiang, X. Chen, *Int. J. Hydrogen Energy* **2014**, 39, 505-531.
263. J. A. Schuler, P. Tanasini, A. Hessler-Wyser, C. Comminellis, J. Van herle, *Electrochem. Commun.*, **2010**, 12, 1682-1685.
264. R. Trebbels, T. Markus, L. Singheiser, *J. Electrochem. Soc.* **2010**, 157, B490-B495.
265. H. Asteman, J. E. Svensson, L. G. Johansson, *Corros. Sci.* **2002**, 44, 2635-2649.
266. H. Asteman, J. E. Svensson, L. G. Johansson, *J. Electrochem. Soc.*, **2004**, 151, B141-B150.
267. P. Piccardo, A. Pecunia, V. Bongiorno, R. Spotorno, *ECS Trans.*, **2015b**, 68, 2611–2624. <https://doi.org/10.1149/06801.2611ecst>.
268. Z. Wuillemin, N. Autissier, A. Nakajo, M. Luong, J. Van herle, D. Favrat. *J Fuel Cell Sci Technol*, **2008**, 5, 011016. <https://doi.org/10.1115/1.2784333>.
269. H. Falk-Windish, J. E. Svensson, J. Froitzheim, *J. Power Sources*, **2015**, 287, 25-35.
270. J. Tallgren, M. Bianco, O. Himanen, O. Thomann, J. Kiviahho, J. Van herle. *ECS Trans.* **2015**, 68, 1597-1608.
271. J. Tallgren, O. Himanen, M. Bianco, J. Mikkola, O. Thomann, M. Rautanen et al. *Fuel Cells* **2015**, 19, 570-577. <https://doi.org/10.1002/fuce.201800169>
272. N. Shaigan, et al, *J. Power Sources*. **2010**, 195, 1529–1542. <https://doi.org/10.1016/j.jpowsour.2009.09.069>.
273. A. Masi, M. Bellusci, S. McPhail, F. Padella, P. Reale, J. E. Hong, R. Steinberger-Wilckens, M. Carlini, *Ceramic Int* **2017**, 43, 2829.
274. Q. Fang, M. Heinrich, C. Wunderlich. Crofer 22 APU in real SOFC stacks, Advances in Solid Oxide Fuel Cells VII, Ceramic Engineering and Science Proceedings, eds N. P. Bansal, P. Singh, S. Widjaja, D. Singh, Hoboken, NJ, USA: John Wiley & Sons, Inc, **2011**, 32.
275. Z. Xu, W. Xu, E. Stephens, B. Koeppel. *Renewable Energy*, **2017**, 13, 1472-1479. <https://doi.org/10.1016/j.renene.2017.06.103>
276. S. Akanda, M. Walter, N. J. Kidner, M. M. Seabaugh, *Thin Solid Films*, **2014**, 565, 237-248. <https://doi.org/10.1016/j.tsf.2014.06.021>
277. B. Deal, A. Grove, *J. Appl Phys*, **1965**, 36, 3770-3778.
278. M. Andersson, J. Yuan, B. Sundén, *Appl. Energy* **2010**, 87, 1461-1476, <http://doi.org/10.1016/j.apenergy.2009.11.013>
279. A. Mai, *ECS Trans.* **2015**, 68, 109-116. <https://doi.org/10.1149/06801.0109ecst>
280. A. Nakajo, F. Mueller, J. Brouwer, J. Van herle, D. Favrat, *Int. J. Hydrogen Energy* **2012d**, 37, 9249-9268.
281. R. Bove, S. Ubertini, *J. Power Sources* **2006**, 159, 543–59. <https://doi.org/10.1016/j.jpowsour.2005.11.045>.
282. J. Van herle, D. Larrain, N. Autissier, Z. Wuillemin, M. Molinelli, D. Favra, *J. Eur. Ceram. Soc.* **2005**, 25(12), 2627-2632.
283. K. Haraldsson, K. Wipke. *J. Power Sources* **2004**, 126, 55–97. <https://doi.org/10.1016/j.jpowsour.2003.08.044>

284. M. Hauck, S. Herrmann, H. Spliethoff, *Int. J. Hydrogen Energy* **2017**, *42*, 10329-10340. <https://doi.org/10.1016/j.ijhydene.2017.01.189>.
285. F. R. Bianchi, B. Bosio, A. Baldinelli, L. Barelli, *Catalysts*, **2020**, *10*, 104. <https://doi.org/10.3390/catal10010104>
286. S. Shen, Y. Kuang, K. Zheng, Q. A. Gao. *Solid State Ion.* **2018**, *315*, 44-51. <http://doi.org/10.1016/j.ssi.2017.11.028>
287. J. Laurencin, F. Lefebvre-Joud, G. Delette, *J. Power Sources*, **2008b**, *177*, 355-368.
288. L. Bernadet, J. Laurencin, G. Roux, D. Montinaro, F. Mauvy, M. Reytier, *Electrochim. Acta* **2017**, *253*, 114-127.
289. E. Lay-Grindler, J. Laurencin, G. Delette, J. Aicart, M. Petitjean, L. Dessemond., *Int. J. Hydrogen Energy*, **2013b**, *38*, 6917-6929.
290. S. Fogel, H. Kryk, U. Hampel, *Int. J. Hydrogen Energy* **2019**, *44*, 9188-9202. <https://doi.org/10.1016/j.ijhydene.2019.02.063>
291. E. Audasso, B. Bosio, S. Nam, *Int. J. Hydrogen Energy* **2016**, *41*, 5571-5581. <https://doi.org/10.1016/j.ijhydene.2015.10.152>
292. B. Conti, B. Bosio, S. J. McPhail, F. Santoni, D. Pumiglia, E. Arato, *Catalysts* **2019**, *9*, 36. <https://doi.org/10.3390/catal9010036>
293. A. Nakajo, F. Mueller, J. Brouwer, J. Van herle, D. Favrat, *Int. J. Hydrogen Energy* **2012e**, *37*, 9269-9286
294. T. Yang, H. Sezer, I. Celik, H. Finklea, K. Gerdes. *ECS Trans.* **2015**, *68*, 239-2411. <https://doi.org/10.1149/06801.2397ecst>
295. M. Gallo, D. Marra, M. Sorrentino, C. Pianese, S. F. Au, *Energy Convers. Manage.* **2018**, *171*, 1514-1528. <https://doi.org/10.1016/j.enconman.2018.06.062>
296. I. Rossi, A. Traverso, D. Tucker, *Appl. Energy* **2019**, *283*, 1543-1550, <http://doi.org/10.1016/j.apenergy.2019.01.092>
297. A. Nakajo, F. Mueller, D. McLarty, J. Brouwer, J. Van herle, D. Favrat, *J. Electrochem. Soc.*, **2011d**, *158*, B1329-B1340.
298. P. Polverino, C. Pianese, M. Sorrentino, D. Marra, *J. Power Sources* **2015**, *280*, 320-338, <http://doi.org/10.1016/j.jpowsour.2015.01.037>
299. P. Polverino, A. Esposito, C. Pianese, B. Ludwig, B. Iwanschitz, A. Mai. *J. Power Sources* **2016**, *306*, 646-657, <http://doi.org/10.1016/j.jpowsour.2015.12.046>
300. M. Sorrentino, C. Pianese, *J. Fuel Cell Sci. Technol.* **2009**, *6*, 0410111-0410112. <https://doi.org/10.1115/1.3081475>
301. M. Guida, F. Postiglione, G. Pulcini, Proc. 9th International Conference on Mathematical Methods in Reliability (MMR 2015), Tokyo, **2015b**, 314-321.
302. M. Guida, F. Postiglione, G. Pulcini. *Commun Statistics Theory Methods* **2019**, *48*, 1748-1765. <https://doi.org/10.1080/03610926.2018.1440306>
303. M. Giorgio, F. Postiglione, G. Pulcini. *Proc. ESREL* **2019**, 707-714, 22-26 https://doi.org/10.3850/978-981-11-2724-3_0317-cd.
304. M. Giorgio, F. Postiglione, G. Pulcini, *Appl Stochastic Models Business Industry*, **2020**, 1-19. <https://doi.org/10.1002/asmb.2522>
305. S. P. S. Badwal, R. Deller, K. Foger, Y. Ramprakash, J. P. Zhang, *Solid State Ionics* **1997**, *99*, 297-310.
306. J. Tor Arne. *Multiple Model Approaches to Modelling and Control*. R. Murray-Smith (Eds.), Taylor and Francis, London, **1997**.
307. Q. Chen, D. R.A. Gao, S. Quan, *J. Power Sources*, **2009**, *191*, 473-482. <https://doi.org/10.1016/j.jpowsour.2009.02.034>. – ISSN 0378-7753
308. A. Marchetti, A. Gopalakrishnan, B. Chachuat, D. Bonvin, A. Tsikonis L Nakajo, Z. Wuillemin, J. Van herle, *J Fuel Cell Sci Technol*, **2011**, *8*, 051001.
309. T. De Avila Ferreira, Z. Wuillemin, A. G. Marchetti, C. Salzmann, J. Van Herle, D. Bonvin. *J. Power Sources* **2019**, *429*, 168-179.
310. T. De Avila Ferreira, Z. Wuillemin, A. G. Marchetti, D. Bonvin. *IFAC-PapersOnLine* **2019c**, *52*, 40-45.
311. J. Zhu, Z. Lin. *Appl. Energy* **2018**, *231*, 22-28, <http://doi.org/10.1016/j.apenergy.2018.09.127>
312. T. Parhizkar, S. Hafeznezami, *Energy Convers.* **2018**, *158*, 81-91, <https://doi.org/10.1016/j.enconman.2017.12.045>
313. M. A. Khaleel, D. R. Rector, Z. Lin, K. Johnson, K. Recknagle, *Int. J. Multiscale Comp. Eng.* **2005**, *3*, 33-47. <https://doi.org/10.1615/IntJMultCompEng.v3.i1.30>
314. L. Mastropasqua, A. Donazzi, S. Campanari, *Fuel Cells* **2019**, *19*, 125-140. <https://doi.org/10.1002/fuce.201800170>
315. M. Mozdierz, K. Berent, S. Kimijima, J. S. Szmyd, G. A. Brus. *Catalysts* **2019**, *9*, 253. <https://doi.org/10.3390/catal9030253>
316. P. Polverino, C. Pianese, *Conf. Control Fault-Tolerant Syst. Sys. Tol.* **2016**, 599-604. <https://doi.org/10.1109/SYSTOL.2016.7739814>
317. T. M. M. Heenan, X. Lu, F. Iacoviello, J. B. Robinson, D. J. L. Brett, P. R. Shearing, *J. Electrochem. Soc.*, **2018**, *165*, F932-F941.
318. M. P. Hoerlein, M. Riegraf, R. Costa, G. Schiller, K. A. Friedrich, *Electrochim. Acta* **2018**, *276*, 162-175. <https://doi.org/10.1016/j.electacta.2018.04.170>
319. O. Ayin, H. Nakajima, T. Kitahara, *Int. J. Hydrogen Energy* **2016**, *41*, 15311-15324. <https://doi.org/10.1016/j.ijhydene.2016.06.194>
320. L. Holzer, B. Münch, B. Iwanschitz, M. Cantoni, T. Hocker, T. Graule, *J. Power Sources* **2011a**, *196*(17) 7076-7089. <https://doi.org/10.1016/j.jpowsour.2010.08.006>
321. M. Hubert. *Ph.D. Thesis*, Université Grenoble Alpes, Grenoble, France, **2016b**.
322. Q. Jeangros, T. W. Hansen, J. B. Wagner, C. D. Damsgaard, R. E. Dunin-Borkowski, C. Hébert, J. Van herle, A. Hessler-Wyser, *Chem. Commun.* **2014a**, *50*, 1808-1810.
323. Q. Jeangros, T. W. Hansen, J. B. Wagner, R. E. Dunin-Borkowski, C. Hébert, J. Van herle, A. Hessler-Wyser, *Acta Mater.* **2014b**, *67*, 363-372.
324. Q. Jeangros, A. B. Aebersold, C. Hébert, J. Van herle, A. Hessler-Wyser, *Acta Mater.* **2016a**, *103*, 442-447.
325. S. P. Jiang, *Int. J. Hydrogen Energy* **2019**, *44*, 7448-7493.
326. T. Klemenso, C. Chung, P. H. Larsen, M. Mogensen, *J. Electrochem. Soc.* **2005**, *152*, A2186-92.
327. D. Marra, M. Sorrentino, C. Pianese, B. Iwanschitz, *J. Power Sources* **2013**, *241*, 320-329. <https://doi.org/10.1016/j.jpowsour.2013.04.114>
328. M. V. MoralesPerez, A. Tarancon, A. Slodczyk, M. Torrell, B. Ballesteros, J. P. Outweltjes, J. M. Bassat, D. Montinaro, A. Morata, *J. Power Sources* **2017**, *344*, 141-151.
329. H. Moussaoui, R. Sharma, J. Debayle, Y. Gavet, G. Delette, J. Laurencin, *J. Power Sources* **2019**, *412*, 736-748. <https://doi.org/10.1016/j.jpowsour.2018.11.095>
330. G. J. Nelson, J. R. Izzo, J. J. Lombardo, W. M. Harris, A. P. Cocco, W. K. S. Chiu, K. N. Grew, A. Faes, A. Hessler-Wyser, J. Van herle, Y. S. Chu, S. Wang. *ECS Trans.* **2011**, *35*, 1323-1327
331. M. Pihlatie, A. Kaiser, M. Mogensen, *Solid State Ionics* **2009**, *180*, 1100-12.
332. P. Polverino, C. Pianese. *Energy Proc* **2017**, *142*, 1706-1713. <https://doi.org/10.1016/j.egypro.2017.12.553>
333. G. Rinaldi, A. Nakajo, J. Van Herle, P. Burdet, E. Oveisi, M. Cantoni, *ECS Trans.*, **2017b**, *78*, 3297-3307.

334. J. A. Schuler, Z. Wuillemin, A. Hessler-Wyser, C. Comminges, N. Y. Steiner, J. Van herle, *J. Power Sources* **2012a**, *211*, 177-183.
335. J. A. Schuler (2012c) 'Chromium Poisoning: The Needle in the SOFC Stack' EPFL PhD thesis no. 5428.
336. Z. Stoynov, D. Vladikova, B. Burdin, *Bulg. Chem. Commun.* **2018a**, *50D*, 21.
337. P. Tanasini, M. Cannarozzo, P. Costamagna, A. Faes, J. Van Herle, A. Hessler-Wyser, C. Comninellis, *Fuel Cells* **2009b**, *9*, 740-752. <https://doi.org/10.1002/fuce.200800192>].
338. D. The, S. Grieshammer, M. Schroeder, M. Martin, M. Al Daroukh, F. Tietz, J. Schefold, A. Brisse, *J. Power Sources* **2015**, *275*, 901-911.
339. D. Waldbillig, A. Wood, D G. Ivey, *Solid State Ionics* **2005**, *176*, 847-59.
340. P. Caliandro, A. Nakajo, S. Diethelm, J. Van herle, *J. Power Sources* **2019**, *436*, 22683-8.
341. M. Cantoni, A. Nakajo, G. Rinaldi, S. Diethelm, J. Van herle, F. Pérez-Willard Characterization of Solid Oxide Electrolysis Cells by Advanced FIB-SEM Tomography, Zeiss White Paper EN_42_013_239, **2017**.
342. T. De Avila Ferreira, Z. Wuillemin, T. Faulwasser, C. Salzmann, J. Van herle, D. Bonvin. *Energy* **2019b**, *181*, 281-293.
343. F. Greco, *EPFL PhD thesis*, **2018**, 8470.

AUTHOR BIOGRAPHIES



Stephen J. McPhail, graduated in Mech Engineering, PhD in thermal fluid dynamics, he is a Researcher at ENEA since 2007, focusing on high-temperature fuel cells and electrolyzers, cell, and system characterization. He is the coordinator of the EERA (European Energy Research Alliance) Joint Programme *Fuel Cells and Hydrogen* and an Italian member of the Technical Collaboration Programme (TCP) *Advanced Fuel Cells* of IEA. He coordinated 4 EU-funded projects (FP7 and H2020) and participated in further 9 EU-funded projects. He is a member of various international Committees on fuel cells and hydrogen (IEC, Mission innovation, IPHE). Co-author of 58 papers on the topic, h-index 17. Winner of 2 IEC "1908" Awards.



Stefano Frangini works at the Energy Department of ENEA CR Casaccia Center as a research scientist in the field of high-temperature materials and corrosion protection techniques for advanced high-temperature electrochemical energy systems. He studied at the University "La Sapienza" of Rome, where he received his degree in Industrial Chemistry in 1986 discussing

a thesis on localized corrosion of structural materials in pressurized water nuclear power plant environments. From 1989, he joined ENEA, where he has been engaged in a broad range of research activities related to materials electrochemistry, corrosion, and protection methods. Current areas of interest focus on analysis of degradation mechanisms in metallic alloys and protective coating materials for high-temperature fuel cell/electrolysis systems.



Dr. Hab. Jérôme Laurencin is a senior scientist at the French Atomic and Alternative Energies Commission (CEA), where he leads a research group on the modeling and characterizations of Solid Oxide Cells (SOC). After a Master degree in material science and engineering, he obtained his Ph.D. from Grenoble Institute of Technology (INPG) with a dissertation on the performance and durability of solid oxide fuel cells. He received his habilitation in 2013 on the modeling of high-temperature electrochemical devices. Jérôme Laurencin has been working on the field of SOC for more than 15 years at CEA. His research activities are related to the modeling coupled with advanced material and mechanical characterizations.



Dr. Effori Elisa attended master's in material science and engineering at the University Of Genoa, Italy. After graduation, she got a PhD in Solid State Electrochemistry and Energy Engineering at the French Atomic and Alternative Energies Commission (CEA) of Grenoble in collaboration with the University of Grenoble Alps. The PhD dissertation was based on the study of the oxygen electrode for Solid Oxide Cells (SOCs) in terms of reaction mechanism and degradation through the use of a modeling tool.



Amira Abaza is an engineer in modeling and scientific computing. After master's degree in applied mathematics, she is currently doing her Ph.D at the French Atomic and Alternative Energies Commission (CEA) in collaboration with the University of Grenoble Alps. Her Ph.D. dissertation is on the fracture of porous ceramics applied to the solid oxide cells (SOC) tech-

nology using modeling coupled with mechanical characterizations.



Aiswarya Krishnakumar Padinjarethil has a master's from KTH Royal Institute of Technology, Stockholm in Chemical Engineering for Energy and Environment. Prior to which she worked as a Process Engineer at the Polypropylene plant at Reliance Industries Limited after receiving her bachelor's degree from the National Institute of Technology, Tiruchirappalli, India. She has been involved in several research projects in the field of catalysis and electrochemistry in Stockholm, Germany, and the United States. In her current studies, she focuses on experimental and statistical analysis of SOC performance under long-term studies.



Prof. Anke Hagen is a chemist with a Dr. rer. nat. from the University of Leipzig and a Dr. techn. from the Technical University of Denmark. International research experiences from Germany, Japan, the United States, and Denmark.

Professional activities comprise, for example, Danish representative in the International Energy Agency IEA: Annex 32, Hydrogen Europe Research, and coordination of SOFC activities at the Department of Energy Conversion and Storage. Responsibilities involve project management, fundraising, teaching, continued education, supervision, and dissemination. Scientific expertise in areas like solid oxide cells, electrochemistry, heterogeneous catalysis, and analytical chemistry.



Daria Vladikova is professor in electrochemistry toward the Bulgarian Academy of Sciences. She has a PhD in Solid State Chemistry and a D.Sc. in Electrochemistry. She is working in the field of Solid Oxide Fuel Cells: testing

monitoring and diagnostics. She is the author of more than 150 scientific publications with 1000 citations, co-author of 6 monographs, and a chapter in Encyclopedia on Power Sources (Elsevier). She has been awarded with Herman Gőhr Award by the European Fuel Cell Forum. Prof. Vladikova is President of the Bulgarian Fuel Cell, Hydrogen and Energy Storage Association

and member of the Governing Board of the European Innovation Digital Hub Zagore.



Blagoy Burdin graduated with master's degree in transport mechanical engineering from Technical University of Sofia. During his dissertation at the same university, he focused on hydrogen fuel cell vehicles. As a PhD student, Blagoy Burdin was a team leader of Technical University Sofia's team in a student competition under which was build both hydrogen and battery-driven vehicles. He graduated PhD with Thesis: "Optimising Electric Vehicle Drive Train using Fuel Cells and Batteries." Currently, Mr. Burdin is a senior assistant professor at the Institute of Electrochemistry and Energy Systems of the Bulgarian Academy of Sciences. His work is related to scientific, applied, and demonstration projects in the field of batteries and fuel cells. His main interests are in the field of electrochemical power sources, renewable energy, and hydrogen fuel cell vehicles.



Fiammetta Bianchi is PhD candidate of chemical, materials, and process engineering at the Department of Civil, Chemical and Environmental Engineering of the University of Genoa (UNIGE). Her research work focuses on green

hydrogen and the use of high-temperature cells, above all solid oxide configuration, for both Gas to Power (fuel cell operation) and Power to Gas (electrolysis mode) applications. The performed activity consists of the modeling of system performance and durability at different phenomenological scales: from the single electrode behavior to stack level.



Barbara Bosio, PhD in Chemical Engineering, is an associate professor of applied physical chemistry at the Department of Civil, Chemical and Environmental Engineering of the University of Genoa (UNIGE). Her main competences concern the detailed simulation of chemical and electrochemical reactors, the analysis of transport phenomena in heterogeneous systems, the identification of kinetic and thermodynamic non-linear parameters.

She is co-author of more than one hundred scientific papers, is a delegate of UNIGE at the European

platform EERA (European Energy Research Alliance) and currently collaborates with research and industrial companies of relevance in the national and international scene.



Paolo Piccardo: University of Genoa (Italy) Delegate of the Rector to the Scientific and Cultural Communication, and the Public Engagement. Associate professor of Metallurgy at the Dept. of Chemistry and Industrial

Chemistry, where he's leading the Metallurgy and Materials Research Group. Ph.D in Chemical Sciences, Professor at Université de Bordeaux Michel de Montaigne (France). He is involved in research activities since 1993 on metallurgy applied to modern and ancient materials focussing on the interaction among materials and between materials and environment. The relationship between chemistry, manufacturing, history, and usage, interactions with other materials of metals have been at the base of research activities dealing with industrial, historical, and archaeological objects believing that metallic materials do not change their behavior according to the period of production but only to the above-mentioned parameters. Ferrous and non-ferrous alloys have been discussed in more than 150 publications and numerous international lectures. Scientific coordinator of numerous industrial financed researches he is active in the field of Li-ion battery: alternative electrodes, recycling, and development of new architectures.; Member of the Panel of Experts of the European Science Foundation; Associate Researcher at INFN (National Institute of Nuclear Physics); Associate Researcher at CNR-ICMATE (Institute of Condensed Matter and Energy, Italian National Council of Researches).



Roberto Spotorno is a researcher of the Department of Chemistry and Industrial Chemistry of the University of Genoa, in the academic field of "Industrial design, machine construction, and metallurgy." He received his PhD in

Chemical Science and Technologies in 2015, with a thesis on "*Development of Stack Components for New Generation Solid Oxide Fuel Cells*". Currently, he is teaching in courses of "Metallurgy" and "Non-ferrous alloys metallurgy" and leads several research activities in the fields of metallurgy, electrochemistry, and materials science applied to energy. His research activity is

mainly focused on the optimization of materials for fuel cells, batteries, and desalination systems.



Hiroyuki Uchida is a Professor of Clean Energy Research Center at the University of Yamanashi and Fellow of the Electrochemical Society (ECS) and the Electrochemical Society of Japan (ECSJ).

His research covers electrocatalysts for fuel cells (PEFCs and SOFCs) and their electrolysis mode (PEWE and SOEC). He has co-authored more than 250 research papers. He has received the Award of the ECSJ, Science and Technology Award of the Ministry of Education, Culture, Sports, Science and Technology (MEXT) of Japan, and the Scientific Achievement Award of the ECSJ.



Pierpaolo Polverino is an assistant professor, Department of Industrial Engineering, University of Salerno. He has an expertise on fuel cells, electrolyzers, and conventional and hybrid vehicles. He has a bachelor's degree

(2007), master's degree (2010), and doctoral degree (2014) with honours in mechanical engineering, University of Salerno. He did an internship (2012) of 9 months at the European Institute of Energy Research (Germany). He is a participant to 11 European Projects (4 ongoing) (FCH JU framework) on modeling, diagnostic, prognostic, and control of fuel cells and electrolyzers. He was awarded in 2019 the Young Scientist Award, from the Hydrogen Europe Research (HER) and FCH JU, and the Outstanding ICAE paper, from Applied Energy."



Ennio Adinolfi, CEO and co-founder of MinervaS, born in 1989. He is a fuel cells and hydrogen specialist, mechanical engineer, and postdoc in advanced monitoring/diagnosis/prognosis tools for automotive and stationary

applications. Lecturer of Smart Industry courses at Aerospace Corporate. Graduated with honors from the University of Salerno. Trained abroad at the European Institute of Energy Research in Germany. He is an active member of the energy committee of the Order of Engineers. He has modeling and programming skills with an interest in green and hi-tech technologies. He

aims at exploiting non-traditional energy sources and business opportunities for reducing global warming.



Fabio Postiglione is currently an Assistant Professor of Applied Statistics at University of Salerno (Italy). He received his Laurea degree (summa cum laude) in Electronic Engineering and his Ph.D. degree in Information Engineering from University of Salerno in 1999 and 2005, respectively. His main research interests include degradation analysis, lifetime estimation, reliability and availability evaluation of complex systems (telecommunication networks, fuel cells), Bayesian statistics, and data analysis. He has co-authored over 120 papers, mainly published in international journals.



Jong-Ho Lee is the leader of the National Research Laboratory (NRL) of Solid Electrolyte Fuel Cell at Korea Institute of Science and Technology (KIST). He has worked as the president of the Solid Oxide Fuel Cell (SOFC) Council of Korean Ceramic Soc. and Technical advisor of Korean SOFC industrialization Forum. He has been involved in many national projects on solid-state ionic device such as SOFC and SOEC. He has worked as an editor of Korean Ceramic Soc. Solid State Ionics and J. Phys. Energy. He has served as a council member of International Soc. of Solid State Ionics (ISSI), TC105 for Fuel Cell Technology, International Electro-Technological Commission (IEC), and TC206 for Fine Ceramics, International Organization for Standardization (ISO).



Dr.-Ing. Hamza Moussaoui is a research scientist at the Swiss Federal Institute of Technology in Lausanne. In 2015, he obtained an Engineering degree in Computational Physics and a research Master's degree in Fluid Dynamics, Energy, and Transfer from the National Polytechnic Institute of Toulouse, France. In 2019, he received his PhD with distinction in Computational Physics applied to Solid Oxide Cells, from Grenoble Institute of Technology, France. His research interests include multi-physics and multi-scale modeling and testing of electrochemical conversion devices in the objective to improve their performance and reliability.



Jan Van Herle, PhD on SOFC cathode materials, 1993, EPFL; Postdoc 1994-5 in Tsukuba, Japan; Scientific collaborator in Chemistry, from 1996, and in Mechanical Engineering from 2000, EPFL; Head of research unit since 2001: 23 completed PhD theses; 60 completed master theses; teaching 5 courses on fuel cells, engines, electrochemistry, thermodynamics, renewable energies, power plants; 340 publications, h-55, from micro to macro, from interfaces to systems, from fundamentals to products, on cell and stack testing and characterization for fuel cells and electrolyzers, 3D microstructural analysis, thermomechanical properties, impedance spectroscopy, catalysis, impurities effects, energy system design and multi-objective optimization.

How to cite this article: Stephen J. McPhail, Stefano Frangini, Jérôme Laurencin, Elisa Effori, Amira Abaza, Aiswarya Krishnakumar Padinjarethil, Anke Hagen, Aline Léon, Annabelle Brisse, Daria Vladikova, Blagoy Burdin, Fiammetta Rita Bianchi, Barbara Bosio, Paolo Piccardo, Roberto Spotorno, Hiroyuki Uchida, Pierpaolo Polverino, Ennio Andrea Adinolfi, Fabio Postiglione, Jong-Ho Lee, Hamza Moussaoui, Jan Van herle. *Electrochem Sci Adv.* **2022**, 2, e2100024. <https://doi.org/10.1002/elsa.202100024>